

See discussions, stats, and author profiles for this publication at: <https://www.researchgate.net/publication/351704343>

# Current development of body-centered cubic high-entropy alloys for nuclear applications

Article in Tungsten · May 2021

DOI: 10.1007/s42864-021-00086-6

CITATIONS

24

READS

391

12 authors, including:



**Tan Shi**

University of Michigan

35 PUBLICATIONS 425 CITATIONS

SEE PROFILE



**Xu Yan**

Xi'an Jiaotong University

16 PUBLICATIONS 167 CITATIONS

SEE PROFILE



**Jing Li**

Xi'an Jiaotong University

5 PUBLICATIONS 73 CITATIONS

SEE PROFILE



**Yundi Zhou**

Shanghai Nuclear Engineering Research and Design Institute

4 PUBLICATIONS 31 CITATIONS

SEE PROFILE



# Current development of body-centered cubic high-entropy alloys for nuclear applications

Tan Shi<sup>1</sup> · Peng-Hui Lei<sup>1</sup> · Xu Yan<sup>1</sup> · Jing Li<sup>1</sup> · Yun-Di Zhou<sup>1</sup> · Yun-Peng Wang<sup>1</sup> · Zheng-Xiong Su<sup>1</sup> · Yan-Kun Dou<sup>2</sup> · Xin-Fu He<sup>2</sup> · Di Yun<sup>1</sup> · Wen Yang<sup>2</sup> · Chen-Yang Lu<sup>1</sup>

Received: 7 February 2021 / Revised: 27 March 2021 / Accepted: 1 April 2021 / Published online: 19 May 2021  
© The Nonferrous Metals Society of China 2021

## Abstract

High-entropy alloys greatly expand the alloy design range and offer new possibilities for improving material performance. Based on the worldwide research efforts in the last decade, the excellent mechanical properties and promising radiation and corrosion resistance of this group of materials have been demonstrated. High-entropy alloys with body-centered cubic (BCC) structures, especially refractory high-entropy alloys, are considered as promising materials for high-temperature applications in advanced nuclear reactors. However, the extreme reactor conditions including high temperature, high radiation damage, high stress, and complex corrosive environment require a comprehensive evaluation of the material properties for their actual service in nuclear reactors. This review summarizes the current progress on BCC high-entropy alloys from the aspects of neutron economy and activation, mechanical properties, high-temperature stability, radiation resistance, as well as corrosion resistance. Although the current development of BCC high-entropy alloys for nuclear applications is still at an early stage as the large design space of this group of alloys has not been fully explored, the current research findings provide a good basis for the understanding and prediction of material behaviors with different compositions and microstructures. Further in-depth understanding of the degradation mechanisms and characterization of material properties in response to conditions close to reactor environment are necessary. A critical down-selection of potential candidates is also crucial for further comprehensive evaluation and engineering validation.

**Keywords** Body-centered cubic high-entropy alloys · Refractory high-entropy alloys · Nuclear materials · Radiation damage · Tungsten

## 1 Introduction

With the increasing demand on energy consumption, it is of great significance to develop advanced nuclear reactor technologies as a long-term plan that can provide carbon-free energies with improved inherent safety, better economic return, higher fuel efficiency, as well as lower long-term environmental impact [1]. The designs of various types of

Generation IV (Gen-IV) nuclear reactors offer appealing features including passive safety measures [2, 3], simpler reactor design [4], higher energy efficiency [5, 6], and better fuel management with a sustainable closed fuel cycle [7, 8]. However, the operating conditions of these reactors pose challenges for the structural materials as they need to withstand a higher span of temperatures (up to ~ 1300 K [1]) and a higher degree of radiation damage (up to 150–200 displacement per atom (dpa) [9]). In addition, the compatibility with corrosive environment, such as molten salts in a molten salt reactor (MSR) [10] or Pb–Bi coolant in a lead-cooled fast reactor (LFR) [11], is also of concern for structural materials in contact with these corrosive media.

Although light water reactors have been commercialized for a long time and there have been ongoing progress for different types of structural materials, it is a challenging problem to develop robust materials for employment in Gen-IV reactors and fusion reactors under extreme reactor

Tan Shi and Peng-Hui Lei have contributed equally to this work.

✉ Tan Shi  
tan.shi0122@xjtu.edu.cn

✉ Chen-Yang Lu  
chenylu@xjtu.edu.cn

<sup>1</sup> Department of Nuclear Science and Technology, Xi'an Jiaotong University, Xi'an 710049, China

<sup>2</sup> China Institute of Atomic Energy, Beijing 102413, China

environment. Conventional austenitic steels have low resistance to radiation-induced swelling [12] and high corrosivity in Pb-alloys at high temperature [13]. Although ferritic/martensitic (F/M) steels have good swelling resistance and can achieve good mechanical performance at high temperature, conventional F/M steels have a higher ductile-to-brittle transition temperature (DBTT) after irradiation, which results in lower ductility and toughness at lower temperature [1, 14]. Oxide dispersion strengthened steel exhibits good overall performance, but suffers from material non-uniformity and high cost of production at large scale [9]. Therefore, there has always been great interest in searching new alternative structural materials for nuclear applications.

In recent years, high-entropy alloys (HEAs) have been considered as promising nuclear materials due to their excellent high-temperature mechanical properties [15, 16], radiation resistance [17–19], and high-temperature corrosion resistance behavior [20]. HEAs are initially defined as alloys with at least five principal elements with the concentration of each element to be within 5–35 at.% [21]. A less strict definition is used later by some where quaternary quasi-equi-molar alloys can also be considered as HEAs or complex concentrated solid-solution alloys (CSAs). With the increase of the alloy system complexity, the configurational entropy  $\Delta S_{\text{config}}$  also increases, and typically when  $\Delta S_{\text{config}}$  is larger than  $1.5R$  ( $R$ : gas constant), the material is considered as a HEA [22]. When  $\Delta S_{\text{config}}$  is between  $R$  and  $1.5R$ , the alloy is classified as medium-entropy alloys (MEAs). Some of the MEAs are also included in this review due to their outstanding properties. The high configurational entropy tends to stabilize the solid solution of the multi-component alloy without the formation of complex phases. The exceptional high-temperature strength and high-temperature stability [23–25] of HEAs originate from their unique intrinsic properties of lattice distortion [25] and sluggish diffusion [26] due to the atomic size mismatch and property difference among different elements. In addition, the HEA properties are not only a simple weighted addition of its constituting elements, the so-called “cocktail effects” reveal that HEA can achieve properties that outperform its constituting elements [27]. The radiation resistance of HEAs have also been demonstrated by atomistic simulations and radiation experiments, and is shown to originate from their unique behaviors on energy dissipation, point defect energetics, and defect cluster evolution [18, 19, 28, 29].

This review examines the potential applications of body-centred cubic (BCC) HEAs as nuclear structural materials. The most important group of BCC HEAs is refractory high-entropy alloys (RHEAs) that are based on refractory element constituents (group IV: Ti, Zr, Hf; group V: V, Nb, Ta; group VI: Cr, Mo, W, etc.) [30]. RHEAs generally have BCC structures with examples such as WNbMoTaV, HfNbTaTiZr and HfMoTaTiZr [31–33]. RHEAs are suitable for

high-temperature applications due to their higher melting temperature and enhanced strength at elevated temperature [31, 34, 35]. Refractory alloys also tend to have good creep resistance and radiation-induced swelling resistance [36]. Although RHEAs tend to be brittle at ambient or low temperature and have oxidation susceptibility, significant progress has been made for the improvement of these properties by alloy design [30, 32, 37–39] and efficient composition-searching strategy [40–42]. Non-refractory elements (Al, Si, or Ni) can also be incorporated into the RHEAs to improve the alloy properties, which further expands the parameter space for alloy design [35]. From the structure perspective, BCC HEAs exhibit a much larger lattice distortion, which could significantly affect their thermodynamic stability and other properties of interests [43]. Motivated by the prospect of BCC HEAs for nuclear applications, this work reviews the current findings on BCC HEAs through the following aspects: neutron economy and neutron activation, alloy preparation and mechanical properties, radiation damage, and corrosion resistance.

## 2 Neutron economy and neutron activation

It is usually undesirable for nuclear structural materials to have a high neutron absorption cross section because if a significant amount of neutrons get absorbed in the non-fuel components, the fuel efficiency is greatly reduced. This is of great importance for components such as fuel cladding, but there could also be exception such as control rod, which is used to intentionally capture neutrons. In the conventional cladding, the thermal neutron absorption cross section of zirconium is as low as 0.185 barn ( $1 \text{ barn} = 10^{-28} \text{ m}^2$ ). Neutron activation refers to the neutron-induced radioactivity of the irradiated materials. Unstable active nuclei can be formed after neutron activation and they will undergo further decay with the emission of different types of radiation. Activated nuclear materials with high radioactivity and long decay time are also undesirable due to the long cooling time, the difficulty in material processing, and their long-term environmental impact [9]. For instance, if new challenges of waste disposal are introduced during the storage, transportation and waste disposal, licensing of cladding materials can be impeded [44]. The neutron absorption cross section and activation behavior are only properties of the nuclei, and their abundance in the designed material determines the overall neutron absorption and activation capability. For HEAs, an examination of the neutron absorption and activation property of all the constituting elements is indispensable.

Although face-centred cubic (FCC) HEAs such as the NiCoFeCrMn system exhibit good resistance to radiation-induced swelling [18], Co has a high thermal neutron

absorption cross section and a long decay time following the neutron activation, which is unsuitable for cladding material in thermal-neutron reactor. Hf, which is present in various RHEAs, also has a large neutron absorption cross section. The demonstration of the radiation resistance of HEAs initiates from projects of fundamental research, but for their actual applications as nuclear structural materials, certain elements need to be better reduced or replaced according to this criterion, which can be done in the initial material design based on the available nuclear data. Figure 1 shows the neutron nonelastic cross section of elements used in both FCC and BCC HEAs [45–54]. The nonelastic cross section corresponds to the difference between the total cross section and the elastic cross section, and is a good reflection of the neutron absorption reactions that are related to the aforementioned problems. Four representative energies (0.025 eV, 1 MeV, 2 MeV, and 14.1 MeV) are chosen due to their relevance for different types of nuclear reactors (thermal-neutron fission reactor, fast-neutron fission reactor, and fusion reactor). It can be seen that elements such as Mn, W, Ta, Co and Hf have large thermal neutron absorption

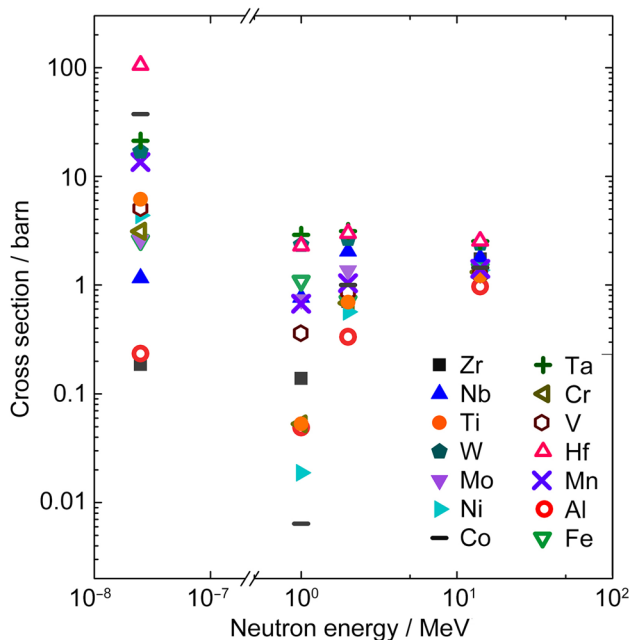


**Fig. 1** Nonelastic cross section of major elements of natural abundance used in FCC and BCC high-entropy alloys. The data are taken from the following nuclear data libraries: Al and Ta (Evaluated Nuclear Data File (ENDF)/B-VIII.0 [45]), Mn (ENDF/B-VII.0 [46]), Cr (ENDF/B-V [47]), V (Chinese Evaluated Nuclear Data Library (CENDL)-3.2 [48]), W (CENDL-3.1 [49]), Zr, Ti and Mo (CENDL-2 [50]), Nb (Joint Evaluated Fission and Fusion (JEFF) Nuclear Data Library-3.3 [51]), Fe and Hf (JENDL-3.2 [52]), Ni (Russian Evaluated Nuclear Data Library: BROND-2.2 [53]), and Co (TALYS-based Evaluated Nuclear Data Library (TENDL)-2019 [54]). We note that the choice of 1 and 2 MeV is beyond the resonance region (except for Fe) where large variations of the cross sections are present

capability, which is not ideal for the neutron economy. The cross section has a strong dependence on the neutron energy, which can result in different absorption capabilities for different types of reactors. For fast reactors, the high neutron absorption cross section is less of a concern compared to thermal reactors. Regarding the issue of neutron activation, not only is the cross section important, but the decay radiations and their corresponding decay times also matter. Activated nuclei that can produce significant radioactivity over a long period of time need to be avoided. The neutron-induced activity after exposure to the first wall of a fusion reactor is shown in Fig. 2 [55]. Although the absorption cross sections do not differ significantly between Nb and other elements shown in Fig. 1, Nb can maintain a much higher radioactivity than other elements after 100 years. For a time frame of 10,000 years, V and Cr can be cooled down to an activity level that is several orders of magnitude lower than the other listed elements, which is definitely an appealing factor. Similar evaluation for other reactor types corresponding to different neutron spectra is also of interest for the further understanding of the activation behaviors of BCC HEAs.

Efforts have been made to exclude high-activation elements in the initial material design. For example, in the work of Et-Atwani et al. [56], high-activation elements such as Ni, Cu, Al, Mo, Co and Nb were excluded to reduce the radioactivity in the scenario of a fusion neutron environment, which led to the ultimate selection of WTaVCr for the irradiation testing. In the work of Kareer et al. [57], Nb in TiVNbTa was replaced by Zr and Cr, which showed comparable hardness

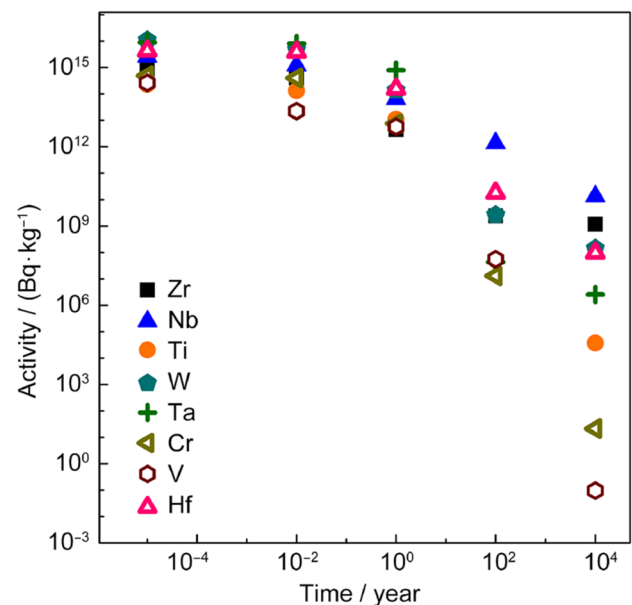


**Fig. 2** Simulated activities of 1-kg pure elements induced by deuterium-tritium fusion neutron spectrum after 5 years of exposure in the reactor first wall. Data are taken from the Handbook of activation data calculated using EASY-2007 [55]

and enhanced irradiation resistance. Elements of V, Cr, Fe, W and Ta were chosen in Ref. [58] due to their low activation properties. By varying Ta and W contents in  $\text{VCrFeTa}_x\text{W}_x$ , it is shown that the microstructures changed from one BCC phase to two BCC and Laves phases, and low contents of Ta and W resulted in excellent hardness and heat softening resistance between 600 and 800 °C. In the work of Sun et al. [59], low-activation elements of V, Cr, Fe, W and Ti were used and the composition was optimized ( $\text{Fe}_{10.78}\text{Ti}_{9.93}\text{Cr}_{8.10}\text{V}_{28.42}\text{W}_{42.77}$ ) to obtain a single BCC solid solution phase. The mechanical properties of the equiatomic and optimized alloy were then compared before and after the homogenization [59]. In the work of Waseem et al. [60], W particles and W fibers were incorporated in the low-activation tungsten alloy  $\text{W}_{0.5}\text{TaTiVCr}$  to improve the matrix ductility for potential use in a fusion plasma environment. A two-fold improvement in compressive fracture strain has been observed with the addition of W particles without significant sacrifice on yield strength, and a four-fold improvement in fracture toughness was demonstrated by the incorporation of W fibers. In addition to HEAs, MEA  $\text{Ti}_{33}\text{V}_{33}\text{Ta}_{34}$  employed elements of low long-term activity and showed high thermal stability after annealing [61]. HEAs offer a wide range of freedom for the tuning of material properties, but also increase the complexity of finding the optimal material design. Although the fundamental research on HEA properties should not be limited to any specific alloy combinations, element-wise down-selection based on the criteria of neutron absorption and activation is essential for nuclear applications.

### 3 Alloy preparation and mechanical properties

#### 3.1 Alloy preparation and microstructures

HEAs are mainly produced by ingot metallurgy such as arc melting [24, 31] and induction melting [62, 63]. Powder metallurgy techniques such as spark plasma sintering [64] and direct metal deposition [65] can also be employed to prepare HEAs [35]. Among the ingot metallurgy methods, arc melting is the most frequently used processing method. Due to the large differences among some of the principal components and the high melting temperature of refractory elements, special care on the homogeneity needs to be taken to reduce the elemental micro-segregation. Long-time annealing of as-cast samples, melting technique with a high solidification rate, multiple times of remelting, and preparation route via powder metallurgy can be used to help achieve a more homogeneous composition [35]. While it is possible to form single-phase BCC structure [66], dendritic structures are frequently present with preferential enrichment

of elements in the dendrite and interdendrite regions [33, 67]. Heat treatment can assist in the homogenization and for alloys with high thermal stability, the BCC solid solution phase will remain unchanged [24, 66, 68, 69]. On the other hand, new phases can also appear after annealing depending on the alloy composition and processing parameters [70].

For RHEAs, single-phase BCC structure is the most common structure due to the high solubility among refractory elements. Examples of the most studied single-phase BCC RHEAs include  $\text{HfNbTaTiZr}$ ,  $\text{MoNbTaW}$ , and their variants, as shown in Table 1. Other structures with more than one phase can also be formed such as BCC and Laves phase (e.g.  $\text{CrNbTiVZr}$  [100]), BCC and ordered B2 phase (e.g.  $\text{Al}_{0.25}\text{NbTaTiZr}$  [118]), and two BCC phases (e.g.  $\text{AlHfNbTaTiZr}$  [119]). Cr element with a small atomic radius favors the formation of the Laves phase due to the reduction in the elastic energy [100, 120]. The Laves phase tends to deteriorate the ductility of the RHEA at room temperature (RT) [62, 100], but good compressive ductility can still be obtained in some cases [70, 106]. Based on current studies, the presence of the ordered B2 phase is associated with Al, Nb, Ta, Ti, and Zr with an enrichment of Al and Zr in the B2 phase [111, 118]. The combined BCC/B2 structure usually shows a good high-temperature strength and thermal stability whereas the B2-based RHEAs without BCC structures (e.g.  $\text{AlNbTiVZr}$ ) have good room-temperature ductility but low strength at high temperature [35]. For  $\text{WNiCo}$ -based HEAs with additions of Cr, Mo and V as principal elements, a disordered FCC structure with dendritic microstructures was observed [121]. The compression ductility is generally good, but the strength depends on the alloy type [121]. In addition to RHEAs, HEAs based on the Cantor alloy ( $\text{FeCrMnNiCo}$  system) can also contain BCC structures. The addition of Al into  $\text{NiCoFeCr}$  can lead to a combined FCC/BCC phase, a combined BCC/B2 phase, or more complicated phases depending on the Al content [110, 115]. Similar structures are also seen from Al-contained Cantor-based HEAs such as  $\text{AlCoCrCuFeNi}$  [122] and  $\text{AlCoCrFeNiSi}_{0.1}$  [123].

Regarding the large production of HEAs, potential problems come from their weak liquidity, castability and homogeneity. It is currently an active research direction to produce HEAs at a large scale. HEAs use similar processing techniques, i.e. ingot metallurgy and powder metallurgy, and casting equipment as conventional alloys, which facilitates the industrial-scale production [27, 124–128]. Currently, kg-scale production of eutectic  $\text{AlCoCrFeNi}_x$  has been demonstrated by induction melting with good chemical homogeneity and mechanical performance [129, 130].

#### 3.2 Mechanical properties

Basic mechanical properties of interest for nuclear structural materials are tensile and creep properties within the

**Table 1** Summary of structures and mechanical properties of BCC high-entropy alloys

Material	Structure	$\sigma_{0.2}$ at RT (MPa)	$\sigma_{0.2}$ at 800 °C (MPa)	$\epsilon_p$ (%) at RT	References
HfNbTiZr	BCC	879 (T)	–	14.9 (T)	[71]
HfNbTaZr	BCC	1315	–	27	[72]
HfNbTiVZr	BCC	1253	–	38	[62]
HfNbTaTiZr	BCC	929 [32]	535 [73]	>50 [32]	[32, 73]
Hf <sub>0.5</sub> Nb <sub>0.5</sub> Ta <sub>0.5</sub> Ti <sub>1.5</sub> Zr	BCC	903	–	17.7	[30]
HfMoNbTiZr	BCC	1719	825	9	[74]
HfMoTaTiZr	BCC	1600	1045	4	[33]
Hf <sub>0.5</sub> Mo <sub>0.5</sub> NbTiZr	BCC	1176	–	24.6	[75]
Hf <sub>0.75</sub> NbTa <sub>0.5</sub> Ti <sub>1.5</sub> Zr <sub>1.25</sub>	BCC	1150	–	>20	[76]
HfMo <sub>0.5</sub> NbTiV <sub>0.5</sub>	BCC	1260	368 at 1000 °C	>30	[77]
HfMo <sub>x</sub> NbTaTiZr ( $x = 0.25, 0.5, 0.75, 1$ )	BCC	1512 ( $x = 1$ )	1007 ( $x = 1$ )	12	[33]
HfMo <sub>0.75</sub> NbTaTiZr	BCC	1370	–	>50	[78]
MoNbTaW	BCC	1058	552	2.6	[24]
MoNbTaV	BCC	1525	–	21	[79]
MoNbTaTiV	BCC	1400	–	30	[80]
MoNbTaTi <sub>x</sub> W ( $x = 0.25, 0.5, 0.75, 1$ )	BCC	1343 – 1455 ( $x = 1$ )	674 ( $x = 1$ )	11.5 – 14.1 ( $x = 1$ )	[38, 67]
MoNbTaTiVW	BCC	1515	791.3	10.6	[67]
MoNbTiV	BCC	1200	–	26	[81]
MoNbTiZr	BCC	1560	–	34	[82]
MoNbTiVZr	BCC	1779	–	32	[83]
Mo <sub>x</sub> NbTiV <sub>0.3</sub> Zr ( $x = 0.1 – 1.5$ )	BCC	1312 ( $x = 0.3$ )	–	50 ( $x = 0.3$ )	[83]
Mo <sub>x</sub> NbTiVZr ( $x = 0.3, 0.5, 0.7, 1.3$ )	BCC	1706 ( $x=0.7$ )	–	32 ( $x = 0.7$ )	[83]
NbTaTiV	BCC	1092	–	>50	[84]
NbTiV <sub>0.3</sub> Zr	BCC	866	–	45	[83]
NbTaTiVW	BCC	1420	–	20	[85]
AlCrMoTi	BCC	–	875	–	[86]
AlNbTiV	BCC	1020	685	5	[87]
AlCoCrFeNi	BCC	1251	–	32.7	[88]
Al <sub>x</sub> CrNbVMo ( $x = 0, 0.5, 1$ )	BCC	2290 ( $x = 1$ )	1070 ( $x = 1$ ) at 1000 °C	15.5	[89]
Al <sub>x</sub> NbTaTiV ( $x = 0.25, 0.5, 1$ )	BCC	1330 ( $x = 0.25$ )	–	46	[84]
Al <sub>0.4</sub> Hf <sub>0.6</sub> NbTaTiZr	BCC	1841	796	10	[90]
Al <sub>x</sub> (HfNbTiZr) <sub>100–x</sub> ( $x = 3, 5, 7, 10, 12$ )	BCC	830.4 ( $x = 5$ ) (T)	–	30 ( $x = 5$ ) (T)	[91]
CrFeMoV	BCC	2730	–	14	[92]
V <sub>0.5</sub> Nb <sub>0.5</sub> ZrTi	BCC	832 (T)	–	18.6 (T)	[93]
Ti <sub>x</sub> ZrVNb ( $x = 1, 1.5, 2$ )	BCC	1086 ( $x = 2$ ) (C) 1058 ( $x = 2$ ) (T)	204 ( $x = 2$ ) (C)	12.3 ( $x = 2$ ) (T)	[94]
Ti <sub>2</sub> ZrHf <sub>0.5</sub> VNb <sub>x</sub> ( $x = 0 – 1$ )	BCC	1065 ( $x = 0.5$ )	135 ( $x = 0.5$ )	>50 (All)	[95]
Ti <sub>8</sub> Nb <sub>23</sub> Mo <sub>23</sub> Ta <sub>23</sub> W <sub>23</sub>	BCC	2377	–	21.3	[96]
Ti <sub>50–x</sub> Al <sub>x</sub> V <sub>20</sub> Nb <sub>20</sub> Mo <sub>10</sub> ( $x = 10, 15, 20$ )	BCC	958 ( $x = 15$ )	550 ( $x = 15$ )	>50 ( $x = 15$ )	[97]
Ti <sub>48</sub> Zr <sub>20</sub> Hf <sub>15</sub> Al <sub>10</sub> Nb <sub>7</sub>	BCC	904 (T)	–	35 (T)	[98]
ZrTiHfV <sub>0.5</sub> Nb <sub>0.5</sub>	BCC	820 (C), 995 (T)	125 (C)	>50 (C), 4.5 (T)	[99]
ZrTiHfNb <sub>0.5</sub> Mo <sub>0.5</sub>	BCC	1195 (T)	595 (C)	>50 (C)	[99]
ZrTiHfNb <sub>0.5</sub> Ta <sub>0.5</sub>	BCC	696 (C), 738 (T)	193 (C)	>50 (C), 8 (T)	[99]
Zr <sub>2</sub> TiHfVNb <sub>2</sub>	BCC	956 (T)	507 (C)	>50 (C)	[99]
NbTiVZr	2BCC	1105	187	50	[100]
MoNbTiV <sub>x</sub> Zr ( $x = 1.5, 2, 3$ )	2BCC	1735 ( $x = 1.5$ )	–	20 ( $x = 1.5$ )	[82]



**Table 1** (continued)

Material	Structure	$\sigma_{0.2}$ at RT (MPa)	$\sigma_{0.2}$ at 800 °C (MPa)	$\epsilon_p$ (%) at RT	References
$\text{Mo}_x(\text{TiZrNbTa})_{100-x}$ ( $x = 0, 5, 10, 15, 20$ )	2BCC	1370 ( $x = 10$ )	–	25 ( $x = 10$ )	[101]
$\text{Al}_x\text{MoNbTaTiV}$ ( $x = 0.2, 0.4, 0.6, 1$ )	2BCC	1352.9 ( $x = 0.6$ )	700 ( $x = 0.6$ ) at 900 °C	21 ( $x = 0.6$ )	[102]
$\text{NbTiV}_2\text{Zr}$	3BCC	918	571	>50	[100]
$\text{Mo}_x\text{NbTiVZr}$ ( $x = 1.5, 1.7, 2$ )	BCC+Laves	1603 ( $x = 1.5$ )	–	20	[83]
$\text{CrNbTiZr}$	BCC + Laves	1260	300	6	[100]
$\text{CrNbTiVZr}$	BCC + Laves	1298	615	3	[100]
$\text{CrTaVW}$	BCC + Laves	2327	979 at 1200 °C	–	[103]
$\text{Cr}_{0.1}\text{Hf}_{0.5}\text{Mo}_{0.5}\text{NbTiZr}$	BCC + Laves	1250	–	31	[104]
$\text{Al}_{0.5}\text{CrNbTi}_2\text{V}_{0.5}$	BCC + Laves	1240	445	>50	[70]
$\text{AlCoCrFeNiTi}_{1.5}$	BCC + Laves	2220	–	5.3	[105]
$\text{AlNbTiVZr}_x$ ( $x = 0.1, 0.25$ )	B2 + $\text{Al}_3\text{Zr}_5$	1360 ( $x = 0.25$ )	855 ( $x = 0.25$ )	8	[106]
$\text{AlNbTiVZr}_x$ ( $x = 0.5, 1, 1.5$ )	B2 + $\text{Al}_3\text{Zr}_5$ + Laves	1485 ( $x = 0.5$ )	675 ( $x = 0.5$ )	>50	[106]
$\text{HfTa}_x\text{TiZr}$ ( $x = 0.4, 0.5, 0.6$ )	BCC+HCP	700 ( $x=0.5$ ) (T)	–	28 ( $x = 0.5$ ) (T)	[107]
$\text{Hf}_{0.5}\text{Mo}_{0.5}\text{NbSi}_x\text{TiZr}$ ( $x = 0.1 - 0.9$ )	BCC + $\text{M}_5\text{Si}_3$	1605 ( $x = 0.5$ )	–	23 ( $x = 0.5$ )	[108]
$\text{HfNbSi}_{0.5}\text{TiV}$	BCC + $\text{M}_5\text{Si}_3$	1399	875	11	[109]
$\text{HfMo}_{0.5}\text{NbSi}_x\text{TiV}_{0.5}$ ( $x = 0.3, 0.5, 0.7$ )	BCC + $\text{M}_5\text{Si}_3$	1617 ( $x = 0.3$ )	398 ( $x = 0.3$ ) at 1000 °C	12.2	[77]
$\text{Hf}_{0.5}\text{Mo}_{0.5}\text{NbTiZrC}_x$ ( $x = 0.1, 0.3$ )	BCC + metal carbide phase	1201 ( $x = 0.3$ )	–	25 ( $x = 0.3$ )	[75]
$\text{Al}_{1.12}\text{CoCrFeNi}$	BCC + B2	1366	–	17	[110]
$\text{AlMo}_{0.5}\text{NbTa}_{0.5}\text{TiZr}$	BCC + B2	2000	1597	11	[90]
$\text{Al}_{0.5}\text{NbTa}_{0.8}\text{Ti}_{1.5}\text{V}_{0.2}\text{Zr}$	BCC + B2	2035	796	4.5	[111]
$\text{Fe}_{34}\text{Cr}_{34}\text{Ni}_{14}\text{Al}_4\text{Co}_4$	BCC + B2	1353	340	40.6	[112]
$\text{Al}_{10}\text{Nb}_{15}\text{Ta}_5\text{Ti}_{30}\text{Zr}_{40}$	BCC + B2	1075	–	55	[113]
$\text{Al}_{0.7}\text{CoCrFe}_2\text{Ni}$	BCC + B2 + FCC	866 (T), 1166 (C)	340 (T) at 1200 °C	5.5 (T)	[114]
$\text{Al}_{0.7}\text{CoCrFeNi}$	BCC + FCC	–	580 (T) at 500 °C	11.5 (T)	[115]
$\text{Al}_{0.5}\text{CrCuFeNi}_2$	BCC + FCC + $\text{L1}_2$	1088 (T)	–	5.6 (T)	[116]
$\text{AlCoCrCuFeNi}$	BCC + FCC + B2 + $\text{L1}_2$	790 (T)	161 (T)	0.2 (T)	[117]
$\text{Al}_{0.74}\text{CoCrFeNi}$	BCC + B2 + FCC	1394	–	24	[110]
$\text{Al}_{0.74}\text{CoCrFeNi}$	BCC + B2 + FCC + $\sigma$	1040 (T)	8 (T)	1 (T)	[117]

(2BCC/3BCC two/three BCC phases, HCP hexagonal close packed). The yield strength ( $\sigma_{0.2}$ ) at RT, the yield strength at 800 °C, and the plastic strain ( $\epsilon_p$ ) at RT are listed. If the measurement at 800 °C is not available, the  $\sigma_{0.2}$  at the closest temperature is shown. The plastic strain at fracture is mostly measured by compressive test (C) and is labeled explicitly for tension test (T)

temperature span of the service environment [131]. For materials with an intermediate level of maturity, a more complete assessment of the mechanical properties needs to be performed including creep-rupture behavior, radiation-induced hardening, stress corrosion cracking (SCC) and irradiation-assisted stress corrosion cracking (IASCC) [132]. In this section, the initial mechanical properties of BCC HEAs are examined. The studies of irradiation effects on BCC HEA mechanical properties are discussed in Sect. 4. Table 1 is a selective list of the mechanical properties of BCC HEAs including both RHEAs and NiCoCrFeAl-based HEAs. The yield strength and plastic strain at fracture at RT are shown to reflect the HEA strength and ductility.

Measurements such as tension/compression test and Charpy impact test can be used to evaluate the ductility of a material. At this stage, the plastic strain at fracture under a quasi-static tensile test along with the analysis of the fracture mode via crack morphology is a good initial evaluation of the material ability to be plastically deformed. As materials in different reactors experience different ranges of temperature (e.g. LFR: ~350–550 °C, very-high-temperature reactor: ~550–1050 °C [9]), a temperature of 800 °C is selected as a compromise to show the material strength at elevated temperature. For advanced reactors, different types of candidate materials (F/M steel, ODS steel, etc.) have different operating temperature windows [9]. Their mechanical performance

can also be found in previous studies for comparison [9, 131–137]. Currently, the creep and fatigue measurements on BCC HEAs are rather limited.

It is known that many alloys with BCC structure suffer from low ductility at RT. Although this is also of concern for BCC HEAs, several alloy systems (e.g. HfNbTaTiZr, MoNbTiVZr, MoNbTiVAl, AlCrNbTiV, AlNbTiVZr, AlNbTaTiZr, NbTiVZr, NbTaTiV and HfMoNbTaTiZr) have shown good compressive strain ( $\epsilon \geq 50\%$ ) at ambient temperature, as presented in Table 1. There are limited studies that performed tension tests where the fracture strain is generally much lower than the compression tests. This difference between compression and tension can be seen from the results of ZrTiHfV<sub>0.5</sub>Nb<sub>0.5</sub> and ZrTiHfNb<sub>0.5</sub>Ta<sub>0.5</sub> where both tests were performed [99]. However, relatively large plastic strain by tension test was also reported for several alloys: 14.9% for HfNbTiZr [71], 28% for HfTa<sub>0.5</sub>TiZr [107], ~30% for Al<sub>0.05</sub>(HfNbTiZr)<sub>0.95</sub> [91], and ~35% for Ti<sub>48</sub>Zr<sub>20</sub>Hf<sub>15</sub>Al<sub>10</sub>Nb<sub>7</sub> [98]. The ductility has a complicated dependence on the elemental composition, phases, and microstructures. While it is easier for dislocations to slip in a single-phase alloy, the slip resistance can also be tuned in multi-phase HEA [97, 106]. The good ductility was reported both at as-cast state [62, 97] and after thermal treatment [83, 100]. Annealing can help achieve a more homogeneous structure, but additional phase can also appear after high-temperature treatment. Nevertheless, thermo-mechanical treatment such as cold work and annealing can be used to enhance the overall HEA strength and ductility [91, 98]. The ductility can be inferred from multiple criteria, such as the valence electron concentration (VEC) [30], the Pugh ratio [138], and the Cauchy pressure. It is found that for single-phase RHEAs with group IV, V, and VI elements, the alloy is intrinsically ductile when VEC is less than 4.5. However, this does not hold for elements from other groups [30, 35]. The Pugh ratio (B/G: ratio of bulk modulus to shear modulus) and the Cauchy constant (the difference of the elastic constants:  $C_{11}-C_{44}$ ) can also be used to predict the alloy ductility [62, 138, 139].

There are quite a lot of BCC HEAs that have demonstrated good room-temperature and high-temperature strength, as shown in Table 1. The tensile strength decreases with increasing temperature with some materials exhibiting a distinct drop-off from a certain temperature [24, 90, 140, 141] and some having a more gradual decrease [73, 74]. Numerous materials have shown excellent yield strength at 800 °C including HfMoNbTiZr [74], MoNbTaTiVW [67], CrTaVW [103], AlNbTiVZr<sub>x</sub> [106], HfNbSi<sub>0.5</sub>TiV [109], and AlMo<sub>0.5</sub>NbTa<sub>0.5</sub>TiZr [90]. Some of these materials maintain high yield strength up to 1000 °C and beyond, such as MoNbTaTiVW, CrTaVW and AlMo<sub>0.5</sub>NbTa<sub>0.5</sub>TiZr [90, 111]. As mentioned previously, it is difficult to achieve a combination of both excellent high-temperature strength and

low-temperature ductility. Among the materials with good ductility at RT, HfNbTaTiZr, TiAlVNbMo, ZrTiHfNbMo, NbTiVZr, and AlNbTiVZr-based HEAs have also presented good strength at elevated temperature. For example, the most studied RHEA HfNbTaTiZr has a yield strength of 535 MPa at 800 °C and a compressive strain larger than 50% [73]. With also a fracture strain larger than 50%, AlNbTiVZr<sub>0.5</sub> showed a yield strength of 675 MPa at 800 °C [106]. We note that the high-temperature performance was not measured in a lot of studies where good ductility was reported. There is indeed a lot of potential for BCC HEAs as the current evaluation of the HEA systems is limited in number and in depth due to a large amount of work required to evaluate a material. According to the existing works, addition of Hf, Zr and Ti in RHEAs is generally believed to improve the ductility whereas Al and V/VI group elements tend to enhance the strength [35]. In addition, the thermo-mechanical process has not been extensively studied for these promising candidate alloys. Designing a ductile matrix with strengthening phases is also a viable way to realize desired properties for nuclear applications.

Different strengthening mechanisms can be used to enhance the mechanical properties of HEAs and CSAs. Various models have been proposed to describe the hardening effect from the intrinsic solid solution strengthening (SSS) of HEAs. The model developed by Labuch [142] for solute-induced stress increase ( $\Delta\sigma_{\text{SSS}}$ ) in binary solid solution has been modified by Senkov et al. [32] to describe the elemental environment in BCC HEAs, which has shown relatively good agreement with the experimental yield stress of HfNbTaTiZr [73] and some other HEAs [80]. According to the Labuch model, the stress increase has two main components: the atomic size misfit parameter  $\delta_a$  and the modulus misfit parameter  $\delta_\mu$ . With the Senkov model, it is found that for HfNbTaTiZr, the atomic size misfit  $\delta_a$  is dominated by interactions of Hf and Zr with other elements while the modulus misfit  $\delta_\mu$  has a larger impact on  $\Delta\sigma_{\text{SSS}}$  and is mainly due to the Ta atom [32]. Other SSS models have also been proposed, which provide different descriptions on interatomic spacing [143], atomic size difference [86], and relationship between  $\Delta\sigma_{\text{SSS}}$  and solute concentration [106, 144]. However, it is also suggested by George et al. [145] that the SSS mechanism is more complicated than a simple extension of the model based on diluted solution. One important difference is that the dominance of the strengthening from screw dislocations for classical BCC metals might not be valid for HEAs [146]. A more complicated model has been developed by Rao et al. [147, 148] based on the Suzuki model of substitutional SSS and atomistic simulations of solute-screw dislocation core interactions. A comprehensive discussion of the underlying mechanism can be found in Ref. [145].

As in conventional alloys, interstitial strengthening, grain boundary strengthening, and precipitation strengthening



can affect the mechanical properties of HEAs as well. The advantage of these methods on HEAs is that there are more degrees of freedom in the compositional space and processing space for the tuning of material properties. The interstitial strengthening effect from carbon has been suggested to affect the WNbMoTaV mechanical properties along with other strengthening mechanisms [34]. The strengthening from oxygen atoms in ZrTiHfNb<sub>0.5</sub>Ta<sub>0.5</sub>O<sub>x</sub> ( $x = 0.05, 0.1, 0.2$ ) has also shown to increase the strength at both ambient and high temperature [149]. Although the ductility decreased with the oxygen content, good compressive fracture strain (>50 %) could still be obtained at an intermediate level of oxygen atoms ( $x = 0.05$  and  $0.01$ ). However, for a lot of studies, the interstitial contamination was rarely measured and was not precisely controlled during the preparation, which makes it difficult to conclude on such effect. The grain boundary strengthening has been studied for HfNbTaTiZr, TiZrHfAlNb, and FeCrNiAlTi<sub>0.2</sub> and was able to achieve both good ductility and strength [98, 150, 151]. For example, the size of the grain boundary could affect the stress-induced martensitic transformation and introduce mechanical twinning in HfNbZrTiAl, which led to the simultaneous increase of the strength and ductility [98]. The precipitation strengthening is an important strengthening mechanism at elevated temperature due to the reduced effect from SSS [35]. As mentioned previously, the Laves phase can enhance the strength but reduce the ductility [100, 105]. The formation of (Hf, Nb, Ti)<sub>5</sub>Si<sub>3</sub> silicide in HfMo<sub>0.5</sub>NbTiV<sub>0.5</sub>Si<sub>x</sub> greatly improved the strength at 1200 °C from 60 MPa at  $x = 0$  to 235 MPa at  $x = 0.7$  with a certain degree of sacrifice on ductility [77]. Hierarchical B2 nanoparticles were observed in the low Co content alloy Fe<sub>34</sub>Cr<sub>34</sub>Ni<sub>14</sub>Al<sub>14</sub>Co<sub>4</sub>, and a fracture strength of 2639 MPa and a compressive strain of 41% were observed owing to the presence of the B2 nanoprecipitates [112].

It can be seen from these studies that BCC HEAs can achieve excellent strength at both RT and high temperature. Promising results on room-temperature ductility have also been demonstrated for multiple alloys. Thermo-mechanical treatment along with the optimization of the alloy composition has shown to be effective in enhancing the ductility, even yielding large elongation under tension deformation [91, 98]. However, most of the measurement were still performed in compression. Ductility at RT with a DBTT below ambient temperature is still one of the major issues for BCC HEAs. Although not discussed in this review, the deformation mechanisms, which are closely related to the intrinsic HEA material properties, have a profound impact on the mechanical behaviors and need to be clearly understood [35, 145]. Although some trends can be observed between the mechanical properties and the choice of elements or the presence of phases, it is rather difficult to make general conclusions, as a lot of processing parameters are not fully

controlled or optimized. Therefore, it is important to carefully control the microstructures, i.e. size and distribution of different phases, via thermo-mechanical treatment to achieve the expected strengthening effect. Due to the large number of possible alloy combinations, a high-throughput discovery or testing scheme seems beneficial with the aid of computational modeling and novel experimental approaches [40, 41].

### 3.3 Thermal stability

Thermal stability, especially microstructural stability, of alloys in long term services at high temperatures is of vital significance. For example, the mechanical properties of alloys containing L1<sub>2</sub> nanoprecipitates are greatly influenced by the morphology, size, and distribution of precipitates [152]. The thermal stability of HEAs is generally evaluated by aging treatment. Aging temperature and time are two key factors that dominate the microstructure and properties of HEAs. The microstructure of HfNbTaTiZr with an initial single-phase BCC structure was investigated as a function of the aging temperature and time [153]. The alloy aged at 600 °C for 15–100 h showed the formation of the (Hf, Ta)-rich HCP phase in the BCC matrix, and similar results were also obtained after aging at 800 °C with a larger size of (Hf, Ta)-rich HCP particles. For the Al<sub>0.4</sub>Nb<sub>0.5</sub>Ta<sub>0.5</sub>TiZr<sub>0.8</sub> with coherent precipitation in the BCC matrix, the spherical B2 nanoprecipitates dispersed in the (Nb/Ta)-rich BCC2 (second BCC phase) matrix were coarsened and showed a cuboidal shape because of an increased lattice misfit after aging at 600 °C for 24 h. When the aging temperature increased to 700–800 °C, the BCC/B2 coherency disappeared, which might be attributed to the formation of the coarse and brittle Zr<sub>5</sub>Al<sub>3</sub> transformed from the ordered B2 nanoprecipitates [154]. The phase stability of Al<sub>0.5</sub>NbTa<sub>0.8</sub>Ti<sub>1.5</sub>V<sub>0.2</sub>Zr with two BCC phases was investigated by Soni et al. [155] at temperatures ranging from 600 to 1000 °C. The aged RHEA was comprised of a continuous BCC matrix with some dispersed B2 precipitates after aging at 600 °C for 120 h. Further, the precipitation of (Al, Zr)-rich HCP intermetallic precipitates in the BCC matrix was observed when the RHEA was aged at 800 and 1000 °C for 20 h. Furthermore, Jia et al. [61] reported that the equiatomic Ti<sub>33</sub>V<sub>33</sub>Ta<sub>34</sub> MEA with a single-phase BCC structure showed high thermal stability with no formation of secondary phases after aging at 400–700 °C for 48 h.

The precipitation of hard  $\rho$  phase (Cr<sub>5</sub>Fe<sub>6</sub>Mn<sub>8</sub>) in Al<sub>x</sub>CrFe<sub>1.5</sub>MnNi<sub>0.5</sub> was observed after up to 100-h aging treatment at 600 °C, displaying an obvious age-hardening [156]. It was reported by Wen et al. [122] that the AlCoCrCuFeNi alloy, which initially had a main BCC phase with some FCC structures, gradually transformed from BCC phase to FCC phase when the aging temperature was above 645 °C. The effect of aging temperature and time on the microstructure

of  $\text{CuCr}_2\text{Fe}_2\text{NiMn}$  HEA was investigated by Ren et al. [157]. An as-cast  $\text{CuCr}_2\text{Fe}_2\text{NiMn}$  HEA consisting of BCC and FCC mixture structure displayed a more homogeneous microstructure, and the precipitation of the  $\rho$  phase transformed from the BCC phase at an aging temperature of 800 °C from 6 to 72 h. However, when the aging treatment temperature increased to 1100 °C, the decomposition of the  $\rho$  phase into the (Cr, Fe, Ni)-rich FCC2 phase (second FCC phase) and the coarsening of the FCC2 phase in the interdendritic regions were observed. Table 2 summarizes the aforementioned studies on the aging. Clearly, these studies indicated that the change in microstructure of HEAs is related to the aging temperature and time. For nuclear applications, the temperature change during the reactor operation has to be taken into account; thus, the mechanical performance of HEAs has to be evaluated after long-term aging to determine their stability at elevated temperatures.

#### 4 Radiation behavior of BCC HEAs

In recent years, the excellent radiation resistance of HEAs and CSAs has been demonstrated, including lower defect production [19, 158, 159], reduced defect growth [160, 161], lower swelling at high temperature [17, 18], reduced helium bubble growth [162, 163] and less extent of

radiation-induced segregation [29]. Most of these studies focused on the FCC Cantor alloy system such as NiCoFeCrMn, and the irradiation studies on BCC HEAs are relatively limited. Based on current studies, the excellent radiation tolerance of HEAs originates mainly from the following aspects: (1) Reduced defect accumulation due to slow energy dissipation. The high degree of chemical disorder and lattice distortion in HEAs increases the electron and phonon scattering, resulting in a lower thermal and electrical conductivity. This will lead to a slower energy dissipation during the collision cascade and a prolonged thermal spike, which further increases the recombination between vacancies and interstitials [19]. Therefore, the number of point defects that escape the initial recombination is greatly reduced. (2) Different behaviors of point defect energetics. First, due to the fluctuation of the atomic local environment and the lattice distortion, the formation and migration energies of vacancy and interstitial atoms exhibit a relatively wide distribution [28]. Next, based on first-principles calculations, it is found that the vacancy migration energy tends to be lower than that of pure metal whereas the interstitial migration energy tends to increase. It is known that interstitials diffuse faster than vacancies. Thus, this change will lead to an overlap of the diffusivity between the two types of point defects, resulting in a higher recombination rate. In addition, atom sluggish diffusion is prominent in HEAs, which has been

**Table 2** Summary of aging studies on BCC HEAs

Material	Initial structure	Aging conditions	Microstructures and mechanical properties	Reference
HfNbTaTiZr	BCC phase	1–100 h at 600–1000 °C	Formation of the (Hf, Ta)-rich HCP phase Increase of hardness at 600 °C at 100 h, no significant increase at 800 °C and 1000 °C	[153]
$\text{Al}_{0.4}\text{Nb}_{0.5}\text{Ta}_{0.5}\text{TiZr}_{0.8}$	Ti/Zr-rich BCC1 and Nb/Ta-rich BCC2	24 h at 600 °C 24 h at 700–800 °C	Coarsened B2 nanoprecipitates $\sigma_{0.2} = 1.232$ GPa (initial: 927 MPa) $\text{Zr}_5\text{Al}_3$ transformed from the B2 nanoprecipitates $\sigma_{0.2} = 934 - 943$ MPa	[154]
$\text{Al}_{0.5}\text{NbTa}_{0.8}\text{Ti}_{1.5}\text{V}_{0.2}\text{Zr}$	Two BCC phases	24 h at 600 °C 20 h at 800–1000 °C	A continuous BCC matrix with discrete B2 precipitates (Al, Zr)-rich HCP intermetallic precipitates and one BCC phase	[155]
$\text{Al}_{0.3}\text{CrFe}_{1.5}\text{MnNi}_{0.5}$	BCC + FCC phase	100 h at 600 °C	$\rho$ phase ( $\text{Cr}_5\text{Fe}_6\text{Mn}_8$ ) transformed from BCC phase hardness from 297 to 850 HV	[156]
$\text{Al}_{0.5}\text{CrFe}_{1.5}\text{MnNi}_{0.5}$	BCC phase	100 h at 600 °C	$\rho$ phase ( $\text{Cr}_5\text{Fe}_6\text{Mn}_8$ ) transformed from BCC phase Hardness from 396 to 890 HV	
AlCoCrCuFeNi	BCC + FCC phase	5 h at 500–1000 °C	Transformation from BCC to FCC phase Increased plastic strain but decreased yield strength	[122]
$\text{CuCr}_2\text{Fe}_2\text{NiMn}$	BCC + FCC phase	6–72 h at 800 °C 12 h at 1100 °C	$\rho$ phase ( $\text{Cr}_5\text{Fe}_6\text{Mn}_8$ ) transformed from BCC phase, improving the homogenization Hardness from 334 to 450 HV Cu-rich FCC phase and (Cr, Fe, Ni)-rich FCC phase Hardness from 334 to 175 HV	[157]

shown to greatly reduce the radiation-induced segregation [29]. (3) Different diffusion dynamics for defect clusters. Due to the alloy complexity, the interstitial clusters tend to have a tortuous three-dimensional diffusion path, in contrast to the one-dimensional diffusion path in pure metals [18]. This will tend to restrict interstitial clusters in the region where vacancies are present and prevent interstitial clusters from reaching distant regions and sinks. In addition to the spatial preference for the migration of defect clusters, their migration energies also differ from pure metals and exhibit a different dependence on the cluster size [18]. When comparing Ni, NiFe, and NiCoCr, the dislocation mobility is shown to be lower with the increase of chemical complexity [160]. It is noted that the atomic size mismatch can not only reduce the diffusion of defects but also produce trapping sites for the facilitation of defect annihilation [164, 165]. Recently, the local chemical ordering has also shown to have a profound impact on the material energy landscape, increasing activation barriers for dislocations and changing their motion pathways [166]. As previously mentioned, these conclusions are mainly drawn from FCC HEAs. While sharing common properties as FCC HEAs, BCC HEAs generally have a larger lattice distortion [167] and different defect structures and behaviors [168, 169], which could lead to different responses to irradiation. It is therefore important to understand whether the aforementioned reasons for the radiation resistance of FCC HEAs still apply for BCC HEAs. Some current studies on BCC HEAs are summarized here in Table 3, which briefly lists the studied material structures, the irradiation or simulation conditions, as well as the main observations and findings.

In the work of Et-Atwani et al. [56], W-based HEA WTaVCr was studied for potential applications in fusion reactors. Elements with high atomic number and high activation were excluded to reduce the sputtering and radioactivity, respectively. An interesting result found from this work is that based on the transmission electron microscopy (TEM) analysis, there was no radiation-induced dislocation-loop discovered under 1 MeV heavy ion ( $\text{Kr}^+$ ) irradiation at 1073 K at a dose rate of  $1.6 \times 10^{-3} \text{ dpa} \cdot \text{s}^{-1}$  and a dose level of 8 dpa. Only V- and Cr-rich precipitates were identified according to TEM and atom probe tomography (APT). The preferential tendency of segregation of Cr and V was explained by a combined *ab initio* and Monte Carlo simulations, which studied the phase stability of different structures and the HEA short-range order. The hardness changed from 14 to 16 GPa at 8 dpa, showing little hardening effect. Partially motivated by this work, Zhao [170] studied the defect energetics of WTaCrV using *ab initio* simulations. The formation and migration energies of different types of vacancies and interstitials were studied. First, regarding the BCC WTaCrV structure, it exhibits a more pronounced lattice distortion than that of FCC HEAs. For the vacancy energetics,

there is a relatively weak correlation between the vacancy formation energy and the types of neighbour atoms or their corresponding displacement during the structural relaxation, except for the Ta atom. It is found that Ta experience the largest relaxation displacement, and vacancy formation energy is lower when more Ta neighbour atoms are present. Interestingly, W atom has a similar large atomic radius but does not lead to the same effect. Regarding the interstitial formation energy, it is lower for interstitial dumbbells containing V and Cr, which can help explain the enrichment of V and Cr and depletion of Ta and W around defect sinks [56]. The interstitial dumbbell favors [110] direction instead of [111] direction in most nonmagnetic BCC metals, which can lead to a lower interstitial diffusivity of WTaCrV. It is found that the structural evolution during the relaxation of an interstitial is complicated, which usually involves change of bond direction, exchange with neighbour atoms and formation of antisite. Based on the aforementioned results and the large overlap between the formation energies of vacancies and interstitials, it is concluded that the increased defect recombination rate will lead to an increased radiation resistance of the material.

A comprehensive irradiation study of FCC and BCC HEAs was performed by Parkin et al. [171] including BCC NbTaTiV, FCC  $\text{Cr}_{18}\text{Fe}_{27}\text{Mn}_{27}\text{Ni}_{28}$ , FCC  $\text{Cr}_{15}\text{Fe}_{35}\text{Mn}_{15}\text{Ni}_{35}$ , along with their corresponding reference metals. The BCC NbTaTiV was irradiated at 50 K at multiple doses up to 2 dpa. At such low temperature, the diffusion of point defects is suppressed so that the experiment provides a clear measurement of the point defect production. As shown in Fig. 3 [171], the saturated defect density in NbTaTiV was approximately 33% of that in pure V due to the slower diffusion and lower point defect production. The difference in defect cluster size between the two materials was statistically insignificant. By comparing FCC and BCC structures under the same irradiation condition, the results imply that larger atomic size mismatch may not lead to greater extent of defect reduction. The similar threshold dpa for defect cluster saturation between V and NbTaTiV also poses questions on the underlying mechanisms for the defect dynamics during the thermal spike and displacement cascade.

While amorphization of metal in solid solution phase under electron irradiation is rare, amorphization induced by fast electrons was observed in BCC  $\text{Al}_{0.5}\text{TiZrPdCuNi}$  by Nagase et al. [172]. It is believed to be due to the high atomic-level stress, which decreases the threshold for the formation of solid solution phase. With a high free energy and a large mismatch in atomic radii, transformation to an amorphous state is facilitated in  $\text{Al}_{0.5}\text{TiZrPdCuNi}$ . Further investigation was also pursued by Odbadrakh et al. [177] where the crystalline phase was found to be unstable with first-principles calculations. In addition, a strong correlation between the charge transfer and atomic-level pressure was

**Table 3** Summary of radiation damage studies on BCC HEAs

Material	Structure	Irradiation/simulation conditions	Observations and findings	Reference
$W_{38}Ta_{36}Cr_{15}V_{11}$	Single-phase BCC	1 MeV $Kr^{2+}$ at 0–8 dpa at 1073 K	No indication of dislocation loops induced by irradiation up to 8 dpa Precipitates enriched in Cr and V Near negligible irradiation hardening	[56]
WTaCrV	BCC special quasirandom structure	128 atoms with a k-point mesh of $3 \times 3 \times 3$	A wide distribution of vacancy and interstitial formation energies Lower migration energy barrier between the Ta atom and vacancy Lower formation energy for interstitial dumbbell with V and Cr The [110] direction favored for interstitial dumbbell Complicated interstitial structural evolution during energy optimization	[170]
Equiatomic NbTaTiV	Single-phase BCC	1 MeV $Kr^{2+}$ ions at 50 K at 2 dpa	Defect cluster size and density as a function of the dpa Reduced defect production of NbTaTiV than pure Nb FCC HEAs also studied at different temperatures (50, 300, and 773 K)	[171]
$Al_{0.5}TiZrPdCuNi$	Single-phase BCC	2 MeV electrons at a flux of $6.7 \times 10^{20} e^- \cdot cm^{-2}$	Solid state amorphization for both coarse and nano-crystalline structure	[172]
Equiatomic HfTaTiVZr	Single-phase BCC	4.4 MeV $Ni^{2+}$ ions at a fluence of $1.08 \times 10^{17} ions \cdot cm^{-2}$ (~30 dpa) at 300 K	Resistant to amorphization up to 30 dpa based on diffraction patterns Less extent of hardening compared with SS304 (28% increase in yield strength vs. 54% increase)	[173]
$Ti_{1.2}ZrHfV_{0.5}Mo_{0.2}$	Single-phase BCC	3 MeV $He^+$ ions at a fluence of $5 \times 10^{15}$ , $1 \times 10^{16}$ , and $3 \times 10^{16} ions \cdot cm^{-2}$ at 873 K	Abnormal lattice constant reduction Higher equilibrium vacancy defects than 316L steel based on PAS Nearly no hardening Similar size but lower density of helium bubbles than traditional alloys	[174]
$V_{2.5}Cr_{1.2}W MoCo_{0.04}$	Single-phase BCC or two BCC phases with similar lattice parameters	5 MeV $Au^+$ , $5 \times 10^{15} ions \cdot cm^{-2}$ (~40 dpa) at 300 K	Phase stability based on EDX Decrease of hardness after irradiation	[175]
Equiatomic HfNbTaTiZr	Not mentioned	300 keV $Ni^+$ at a fluence of $1.5 \times 10^{16} ions \cdot cm^{-2}$ (~30 dpa) at 373 K	A swelling ratio of 1.23% Negligible hardening	[176]

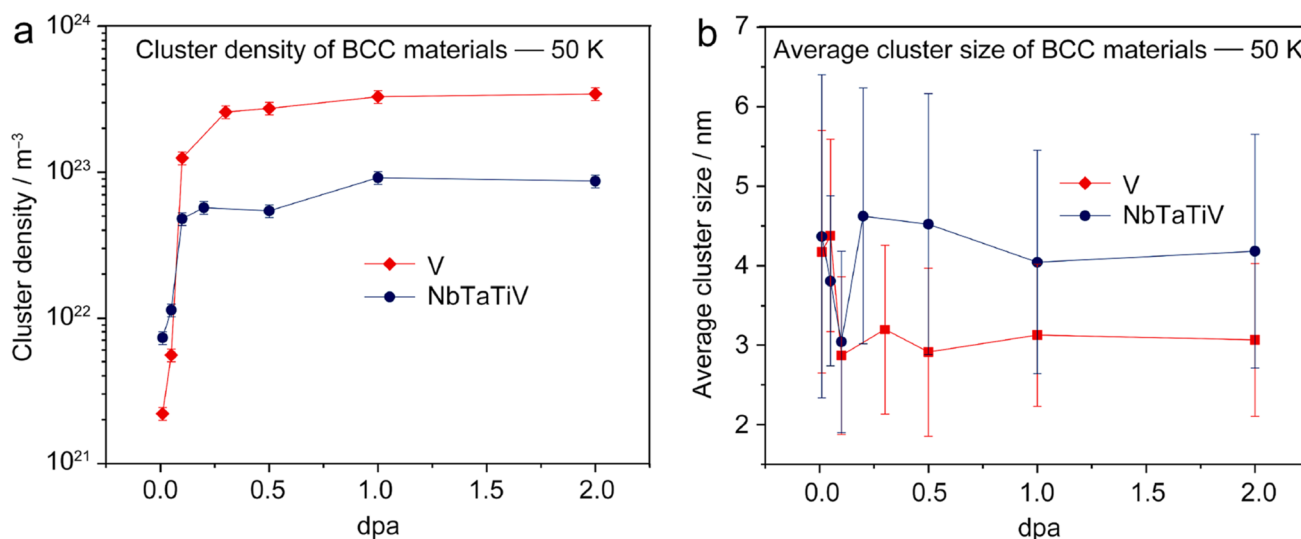


**Fig. 3** Comparison of the **a** defect cluster density and **b** average defect cluster size of V and NbTaTiV at 50 K. Reproduced with permission from Ref. [171]. Copyright 2020 Elsevier

discovered for the glassy phase, showing that atomic-level stress was not only controlled by the atomic size, but also by the local charge transfer. An earlier study from the same group of Nagase et al. [178] used similar methodology to irradiate MEA  $\text{Zr}_{20.8}\text{Hf}_{45.5}\text{Nb}_{33.7}$  with 2 MeV electrons at 103 K and 298 K. The phase stability of ZrHfNb against irradiation and the dependence of critical dose of amorphization on temperature were discussed in that work.

Sadeghilaridjani et al. [173] compared HfTaTiVZr and SS304 stainless steel under the same irradiation condition and found that the hardening of HfTaTiVZr was only approximately 40% of SS304. In addition, HfTaTiVZr kept a BCC crystalline structure at a dose level of 20–25 dpa. A combination of crystalline and amorphous phases only appeared beyond a dose level of 30–40 dpa, which is better than those of typical intermetallic compounds and other refractory metals [179, 180]. Lu et al. [174] irradiated  $\text{Ti}_2\text{ZrHfV}_{0.5}\text{Mo}_{0.2}$  by helium ions at a high temperature of 873 K. In contrast to the expected swelling behavior, the lattice parameter of irradiated HEA was decreased by 0.676%, which is speculated to be due to the large lattice distortion. The vacancy concentration was found to be larger than the corresponding pure metals and binary alloys based on positron annihilation spectroscopy (PAS) [181], which is believed to affect the helium bubble growth due to the interactions between vacancy defects and helium atoms. Along with the results of negligible hardening and lower density of helium bubbles, the interrelations of these interesting findings need to be further explored. In the study of Patel et al. [175], the as-cast  $\text{V}_{2.5}\text{Cr}_{1.2}\text{WMoCo}_{0.04}$  exhibited a dendritic microstructure with preferential segregation of V and Cr at inter-dendritic regions. The as-cast sample was

then irradiated by heavy ions and showed relatively stable phase stability based on XRD and energy dispersive X-ray (EDX) spectroscopy with 4 wt.% phase transformation into a similar BCC phase. The measured Vickers microhardness changed from  $9.47 \pm 1.08$  GPa at the as-cast state to  $7.55 \pm 0.18$  GPa after irradiation. The unexpected decrease in hardness is speculated to originate from the annealing of intrinsic and radiation-induced defects. In the work of Chang et al. [176], HfNbTaTiZr was irradiated by 300 keV  $\text{Ni}^+$  ions with over 30 dpa in the peak damage region. At 373 K, a swelling ratio of 1.23% was determined, which is similar to that of FCC  $\text{Al}_{0.1}\text{CoCrFeNi}$  [182]. It is known that the swelling is highly temperature-sensitive and becomes prominent during the intermediate temperature range. Thus, the swelling behavior at higher temperatures needs to be explored. The hardness was measured to be  $3.6 \pm 0.3$  and  $3.5 \pm 0.4$  GPa for the initial and irradiated sample, respectively, showing negligible hardening effect.

In addition to these works that directly studied BCC HEAs, there are also several works that are relevant to the radiation resistance of BCC HEAs. Jiang et al. [183] discovered that the FCC NiFeCoCrCu can produce alternating layers of FCC and BCC structures of nanometer thicknesses. Irradiation with 3 MeV Ni ions was performed from low dose up to 370 dpa, and the nano-laminate structure was extensively analyzed by TEM and APT. Although starting from a FCC HEA, the results demonstrate a controlled method for producing layered dual-phase structure and an increased radiation resistance of HEA by introducing BCC phase. Egami et al. [184] simulated the dependence of amorphization on dpa for multi-component alloys and predicted that solid solution at the boundary of amorphous phase with



a high level of atomic-level strain would exhibit good radiation resistance.

Some of these works show very exciting results on the radiation resistance of BCC HEAs. However, the related studies on BCC HEAs are rather limited, and more in-depth and more systematic studies including the characterization of defect microstructures are required to help fully understand mechanisms that affect the radiation resistance of these materials. More specifically, it is important to know whether the energy dissipation during the collision cascade, the point defect energetics, and the defect cluster dynamics follow the same behavior as FCC HEAs. We note that radiation conditions such as ion species, dose rate, and temperature play a crucial role on the defect recombination and evolution. For example, the swelling behavior is highly temperature-dependent; the electron and heavy ion irradiation lead to cascade of different sizes and large temperature shift relative to neutrons. Most of these works focused on heavy ion irradiation while proton and neutron irradiation are still missing. A comprehensive comparison of the observed property change with other conventional nuclear materials is important for an unbiased evaluation of the radiation response. HEAs offer a wide range of options for exploration, but critical evaluation of these materials seem to be essential for the down-selection of promising candidates.

## 5 Resistance to corrosion

For nuclear materials, a high degree of chemical compatibility with the corresponding corrosive media at reactor service temperature is extremely important for their reliable use during the long period of service time [185]. Taking LFR as an example, there is a continuous interest in increasing the operating temperature to increase the reactor efficiency. Although oxygen concentration is usually controlled in the lead or lead-bismuth eutectic (LBE) coolant to form the protective oxide film to reduce the metal dissolution, austenitic steels can still experience heavy dissolution at elevated temperatures and are also not suitable for high-dose components. While F/M steels (9–12% Cr) are considered as promising candidates for LFR, the thermal conductivity can be degraded by the thick oxide when the temperature is above 550 °C, which is also potentially unstable [1, 186]. Regarding the high-temperature candidates, conventional refractory elements have low oxidation resistance and low fracture toughness [186]. Beyond the traditional routes of optimizing the element content (Si, Al, etc.) [187, 188], the concept of HEAs has the potential to break through the design limitation of conventional alloys, improving the corrosion resistance and mechanical properties simultaneously. HEAs have been considered as promising candidate materials for the accident-tolerant fuel (ATF) cladding of

nuclear reactors and the storage containers of the long-term/interim disposal nuclear waste due to their promising corrosion resistance [189–193]. It is noted that different corrosion reactions and mechanisms are involved in different corrosive media, which imposes different constraints on the alloy design. For example, in contrast to LFR, the electrochemical corrosion is more important in a MSR environment, where the formation of stable oxide film is less likely and elements such as Ni and Cr have different impact on the corrosion resistance compared to that of Pb/LBE coolant [194].

Corrosion resistance of  $\text{Al}_{0.7}\text{CoCrFeNi}$  in Pb-Bi medium was studied for the potential use in the LFR. Gong et al. [115] studied the liquid metal embrittlement (LME) of the dual-phase  $\text{Al}_{0.7}\text{CoCrFeNi}$  HEA (FCC + BCC) in LBE at 350 °C and 500 °C. The  $\text{Al}_{0.7}\text{CoCrFeNi}$  was selected due to the overall good performance in strength and ductility. However, there was a significant ductility loss in LBE in comparison with the experiment in air. The embrittlement was observed at both temperatures with cracks propagating mostly within the BCC phase at 350 °C and at BCC/FCC phase boundaries at 500 °C. It is concluded that the (Ni, Al)-rich BCC phase is susceptible to LME whereas the (Co, Cr, Fe)-rich FCC phase is immune to LME [115].

Although the discussion of BCC HEAs is mostly envisioned for advanced reactors,  $\text{AlCrMoNbZr}$  has also been studied as the coating material of N36 zirconium alloy for the fuel cladding of light water reactors [189]. The addition of a protective coating is motivated by the concept of ATF to reduce the risk of zirconium oxidation and hydrogen gas release during a loss-of-coolant accident, as evidenced by the Fukushima accident. The  $\text{AlCrMoNbZr}$  coating was found to be well adhered to the substrate by magnetron co-sputtering and showed a high hardness of 11.8 GPa. For a 30-day corrosion test of  $\text{AlMoNbVZr}$  coating in static pure water at high pressure (18.7 MPa) and at high temperature (360 °C), the coating maintained a strong bonding to the N36 zirconium alloy with the formation of a complex protective film consisting of  $\text{Nb}_2\text{Zr}_6\text{O}_{17}$ ,  $\text{ZrO}_2$ , and  $\text{Cr}_2\text{O}_3$ , showing the enhancement of the corrosion resistance by the  $\text{AlCrMoNbZr}$  coating [189].

Besides the aforementioned investigations, the other corrosion studies are not targeted to nuclear reactor environment. The experiments were usually conducted at RT in a Cl-containing or acid solution. However, these works are useful for understanding the general corrosion behaviors of BCC HEAs and could be relevant for the storage of nuclear waste and the water-based nuclear reactors. For example, during the dry cask storage of spent nuclear fuel near the power plants, there can be corrosion problems from NaCl due to its proximity to the sea. During the long-term disposal of nuclear waste, it is also important to ensure the resistance to underground water of different chemical conditions. The relevant corrosion studies of BCC HEAs are discussed



here mainly through three aspects: elemental compositions, microstructures, and surface conditions. First, the impact of various elements on the corrosion resistance has been investigated. An optimal amount of Al in VNbMoTaWAl coating has shown to enhance both the mechanical properties and corrosion resistance in the  $\text{H}_2\text{SO}_4$  solution [195]. The addition of Cr and B in the NbMoTaW coating has shown to enhance the corrosion performance in a 3.5 wt.% NaCl solution [196]. The pitting resistance and general corrosion resistance of  $\text{TiZr}_{0.5}\text{NbCr}_{0.5}\text{V}_x\text{Mo}_y$  exhibited different behaviors in NaCl and  $\text{H}_2\text{SO}_4$  solution with the addition of V and Mo contents due to the nature of the passive film and the dispersion of  $\text{Cr}_2\text{Zr}$  precipitation [197]. In contrast to RHEAs, the addition of Al is not beneficial in NiCrFe-based system. In  $\text{Al}_x\text{CoCrFeNi}$  ( $x = 0.3, 0.5$  and  $0.7$ ) alloys, an increase in Al content has shown to deteriorate the corrosion resistance in the NaCl solution due to the increase of the Cr-depleted, (Al, Ni)-rich BCC phase, resulting in the formation of thick dispersive passive films that facilitate the attacks from  $\text{Cl}^-$  ions [198]. Nevertheless, the pitting potential of  $\text{Al}_x\text{CoCrFeNi}$  is high compared with conventional alloys, as shown in Fig. 4 [198]. The negative impact of the addition of Al was also reported in the  $\text{Al}_x\text{CoCrFeNi}$  ( $x = 0, 0.25, 0.5$  and  $1.0$ ) [199] and  $\text{Al}_x\text{CrFe}_{1.5}\text{MnNi}_{0.5}$  ( $x = 0, 0.3, 0.5$ ) [200]. While boron can increase the HEA hardness and wear resistance in  $\text{Al}_{0.5}\text{CoCrCuFeNi}$ , it was shown to degrade the corrosion resistance in the  $\text{H}_2\text{SO}_4$  solution with more localized attacks on the boride precipitates [201].

Inhomogeneous microstructure and elemental segregation have a great impact on the corrosion resistance of HEAs. The presence of second phase and elemental segregation that are prone to corrosion can greatly weaken

the localized corrosion resistance and promote the microgalvanic attack [191, 202]. Homogeneous structure is found to be beneficial for RHEAs [192, 193, 203]. For example, TaNbHfZrTi exhibited low corrosion rate in both 3.5 wt.% NaCl solution [192] and boiling  $\text{HNO}_3$  (120 °C) [203] accredited to its single-phase BCC structure. The single-phase BCC  $\text{TiCrVNb}_{0.5}\text{Al}_{0.5}$  with a homogeneous element distribution also exhibited low corrosion density, high repassivation ability, and high breakdown potential in both NaCl and HCl solutions [193]. The formation of dendritic microstructure with interdendritic phases can be detrimental for the HEA corrosion behavior. As mentioned previously, the Cr-depleted dendrites in AlCoCrFeNi are prone to corrosion attacks [198]. In contrast, the BCC AlCoCrFeNi coating prepared by electrospray deposition showed negligible intercellular segregation and therefore exhibited significantly better corrosion resistance than the as-cast HEA and the AISI 1045 carbon steel substrate [204]. The detrimental effect of interdendritic microstructure was also observed for other Cantor alloys with BCC structures [123, 201].

The multiple principle components of the HEAs complicate the chemical composition and morphology of the surface film. For  $\text{Hf}_{0.5}\text{Nb}_{0.5}\text{Ta}_{0.5}\text{Ti}_{1.5}\text{Zr}$ , the corrosion resistance was shown to be significantly better than 316 L stainless steel in the 3.5 wt.% NaCl solution [192]. A continuous, stable passive film of  $\text{TiO}_2$ ,  $\text{ZrO}_2$ ,  $\text{HfO}_2$ ,  $\text{Nb}_2\text{O}_5$ ,  $\text{Ta}_2\text{O}_5$ , and metallic Ta was formed. Besides the contribution from a homogeneous structure and a higher content of passivity-promoting elements, the metallic Ta and the presence of  $\text{OH}^-$  could help repair the passive film [192].  $\text{TiCrVNb}_{0.5}\text{Al}_{0.5}$  also exhibited good corrosion resistance in a chloride environment with the formation of a passive film with a high concentration of  $\text{Cr}_2\text{O}_3$ ,  $\text{TiO}_4$ , and  $\text{Al}_2\text{O}_3$ . In addition, it is found that  $\text{Ti}^{4+}$  assisted in the repassivation, and the formation of  $\text{Ti}^{4+}$  was promoted by the presence of  $\text{Nb}^{5+}$  [193, 205]. On the other hand, the formation of certain compounds deteriorates the protective passive film. In fluorinated nitric acid, the TaNbHfZrTi experienced significant corrosion owing to the formation of  $\text{ZrF}_4$ ,  $\text{ZrOF}_2$ , and  $\text{HfF}_4$ , showing the negative impact of Hf and Zr [203]. For  $\text{Al}_{0.5}\text{CoCrCuFeNiB}_x$ , the formation of  $\text{CrB}_2$ ,  $\text{Co}_2\text{B}$ , and  $\text{FeB}$  reduced the coverage of  $\text{Cr}_2\text{O}_3$  passive film [206].

These existing works provide a good basis for the understanding of corrosion behaviors of BCC HEAs. However, the studies related to nuclear applications are scarce. For the potential uses as nuclear materials, it is crucial to test these materials under conditions close to the reactor environment. The chemical conditions for different types of reactor also need to be considered. The aforementioned studies mostly focused on ambient temperature testing, but the corrosion mechanisms and dynamics could

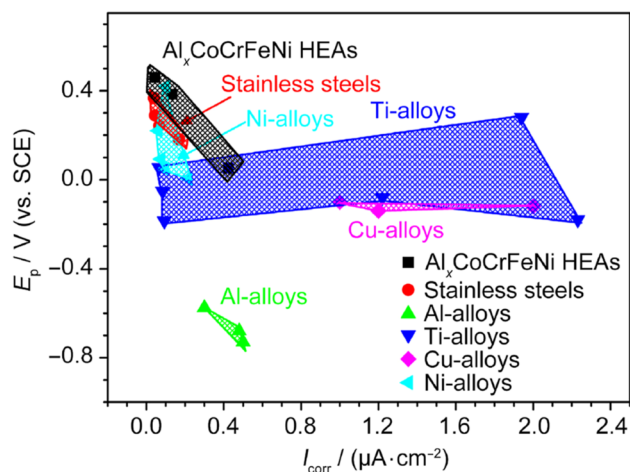


**Fig. 4** Critical pitting potential ( $E_p$ ) vs. saturated calomel electrode (SCE) as a function of the corrosion current density for  $\text{Al}_x\text{CoCrFeNi}$  HEAs and conventional alloys at RT in 3.5 wt.% NaCl solution. Reproduced with permission from Ref. [198]. Copyright 2017 Elsevier

be completely different at high temperatures. The corrosion performance is also entangled with other factors, such as SCC, IASCC, and the production of fission products, which makes the corrosion failure a rather complicated and challenging issue. Thus, future investigation is needed to fully understand chemical durability and corrosion resistance of the BCC HEAs for nuclear applications.

## 6 Conclusions and outlook

For nuclear applications, although it is desirable for the material to have outstanding performance in all areas, the selection criteria usually lead to the choice of materials having overall balanced properties due to the considerations and limitations from different aspects. One of the motivations of this review is to provide a global view on these aspects, which allows a more efficient and prudent pathway for the material search. For the potential use of BCC HEAs in advanced nuclear reactors, the elements that can induce high neutron activation need to be better reduced or avoided. The high neutron absorption cross section is also of great concern for critical components in thermal neutron reactors. Multiple BCC HEAs have shown excellent mechanical strength at elevated temperatures, and some have also shown good room-temperature compression ductility. However, tension tests are rarely performed and DBTT below RT needs to be determined. The improvement of room-temperature ductility relies on the understanding of strengthening and deformation mechanisms, controlling of the thermo-mechanical process, as well as an efficient way of exploration among this large material family. While multiple studies have demonstrated the great radiation tolerance of FCC HEAs, it is yet to be determined whether the same mechanisms apply to BCC HEAs and how they differ from the former. Current atomistic simulations have shown that due to the larger extent of lattice distortion and difference in electronic properties, the point defect behaviour is different from that of Cantor alloys. Although promising results on the radiation tolerance of BCC HEAs have been reported, further comprehensive studies on microstructure characterization and mechanism understanding are indispensable. The current corrosion studies investigated mostly the impact of elements and microstructures at RT, whereas experiments at high temperature and under reactor environment, such as lead-bismuth medium, are still scarce.

At this early stage of development of BCC HEAs, it is important to first understand the basic material performance and basic degradation mechanisms in response to these individual environmental factors. A great challenge is the limited number of studies on each alloy system

where a systematic evaluation can be hardly formed due to the difference in material microstructures, experimental conditions, characterization methods, etc. Therefore, theories that can explain and predict the common behaviors of BCC HEAs or at least a group of BCC HEAs are instructive. A delicate balance needs to be achieved between an exploratory search among  $\geq 10,000$  alloy systems and a more focused investigation on promising candidates based on application-oriented requirement. High-throughput computational and experimental approaches are therefore required for the quick discovery among the vast design and compositional space. Although high-throughput screening tests have a higher degree of uncertainty than conventional tests, they allow a faster examination among HEAs. In addition to BCC HEAs, some BCC MEAs also exhibited excellent mechanical performance with high-temperature stability, which requires further exploration [61]. After a clear understanding of these basic mechanisms, evaluation of promising material candidates at conditions close to reactor environment, such as neutron irradiation at test reactors, is needed at the next stage to fully understand their potential for advanced reactors.

**Acknowledgements** This work was supported by the National Key Research and Development Program of China (Grant Nos. 2019YFA0209900 and 2017YFB0304403); the National Natural Science Foundation of China (Grant No. 12075179); the Nuclear Material Technology Innovation Center Project (Grant No. ICNM 2020 ZH05); and the Continuous Basic Scientific Research Project (Grant No. WDJC-2019-10). We would like to thank Prof. Shao-Qiang Guo for the suggestion on the corrosion section of this review.

## References

1. Yvon P, Carré F. Structural materials challenges for advanced reactor systems. *J Nucl Mater.* 2009;385(2):217.
2. Chen H, Chen Z, Chen C, Zhang X, Zhang H, Zhao P, Shi K, Li S, Feng J, Zeng Q. Conceptual design of a small modular natural circulation lead cooled fast reactor SNCLFR-100. *Int J Hydrogen Energy.* 2016;41(17):7158.
3. Aoto K, Dufour P, Hongyi Y, Glatz JP, Kim YI, Ashurko Y, Hill R, Uto N. A summary of sodium-cooled fast reactor development. *Prog Nucl Energy.* 2014;77:247.
4. Duffey R. The development and future of the supercritical water reactor. *CNL Nucl Rev.* 2016;5(2):181.
5. Smith CF, Halsey WG, Brown NW, Sienicki JJ, Moiseyev A, Wade DC. Sstar: the US lead-cooled fast reactor (LFR). *J Nucl Mater.* 2008;376(3):255.
6. Stainsby R, Peers K, Mitchell C, Poette C, Mikityuk K, Somers J. Gas cooled fast reactor research in Europe. *Nucl Eng Des.* 2011;241(9):3481.
7. Cinotti L, Smith CF, Sekimoto H. Lead-cooled fast reactor (LFR) overview and perspectives. Lawrence Livermore National Lab. (LLNL), Livermore, CA (United States). Tech. rep. 2009.
8. Van Rooijen W, Kloosterman J, Van Der Hagen T, Van Dam H. Definition of breeding gain for the closed fuel cycle and application to a gas-cooled fast reactor. *Nucl Sci Eng.* 2007;157(2):185.

9. Zinkle SJ, Busby JT. Structural materials for fission & fusion energy. *Mater Today*. 2009;12(11):12.
10. Zheng G, Sridharan K. Corrosion of structural alloys in high-temperature molten fluoride salts for applications in molten salt reactors. *JOM*. 2018;70(8):1535.
11. Ballinger RG, Lim J. An overview of corrosion issues for the design and operation of high-temperature lead-and lead-bismuth-cooled reactor systems. *Nucl Technol*. 2004;147(3):418.
12. Cawthorne C, Fulton E. Voids in irradiated stainless steel. *Nature*. 1967;216(5115):575.
13. Sapundjiev D, Van Dyck S, Bogaerts W. Liquid metal corrosion of T91 and A316L materials in Pb-Bi eutectic at temperatures 400–600 °C. *Corros Sci*. 2006;48(3):577.
14. Klueh R, Nelson AT. Ferritic/martensitic steels for next-generation reactors. *J Nucl Mater*. 2007;371(1–3):37.
15. Ding Q, Zhang Y, Chen X, Fu X, Chen D, Chen S, Gu L, Wei F, Bei H, Gao Y, Wen M, Li J, Zhang Z, Zhang Z, Zhu T, Ritchie RO, Yu Q. Tuning element distribution, structure and properties by composition in high-entropy alloys. *Nature*. 2019;574(7777):223.
16. Li TC, Lv YB, Cao ZJ, Yu TM, Li TJ. Opportunity and challenge of refractory high-entropy alloys in the field of reactor structural materials. *Acta Metall Sin*. 2020;57:42.
17. Jin K, Lu C, Wang L, Qu J, Weber W, Zhang Y, Bei H. Effects of compositional complexity on the ion-irradiation induced swelling and hardening in ni-containing equiatomic alloys. *Scripta Mater*. 2016;119:65.
18. Lu C, Niu L, Chen N, Jin K, Yang T, Xiu P, Zhang Y, Gao F, Bei H, Shi S, He MR, Robertson IM, Weber WJ, Wang L. Enhancing radiation tolerance by controlling defect mobility and migration pathways in multicomponent single-phase alloys. *Nat Commun*. 2016;7(1):1.
19. Zhang Y, Stocks GM, Jin K, Lu C, Bei H, Sales BC, Wang L, Béland LK, Stoller RE, Samolyuk GD, Caro M, Caro A, Weber WJ. Influence of chemical disorder on energy dissipation and defect evolution in concentrated solid solution alloys. *Nat Commun*. 2015;6(1):1.
20. Shi Y, Yang B, Liaw PK. Corrosion-resistant high-entropy alloys: a review. *Metals*. 2017;7(2):43.
21. Yeh JW, Chen SK, Lin SJ, Gan JY, Chin TS, Shun TT, Tsau CH, Chang SY. Nanostructured high-entropy alloys with multiple principal elements: novel alloy design concepts and outcomes. *Adv Eng Mater*. 2004;6(5):299.
22. Zhang W, Liaw PK, Zhang Y. Science and technology in high-entropy alloys. *Sci China Mater*. 2018;61(1):2.
23. Hsu CY, Juan CC, Wang WR, Sheu TS, Yeh JW, Chen SK. On the superior hot hardness and softening resistance of AlCoCr<sub>0.5</sub>FeMo<sub>0.5</sub>Ni high-entropy alloys. *Mater Sci Eng A*. 2011;528(10–11):3581.
24. Senkov ON, Wilks G, Scott J, Miracle DB. Mechanical properties of Nb<sub>25</sub>Mo<sub>25</sub>Ta<sub>25</sub>W<sub>25</sub> and V<sub>20</sub>Nb<sub>20</sub>Mo<sub>20</sub>Ta<sub>20</sub>W<sub>20</sub> refractory high entropy alloys. *Intermetallics*. 2011;19(5):698.
25. Lee C, Song G, Gao MC, Feng R, Chen P, Brechtl J, Chen Y, An K, Guo W, Poplawsky JD, Li S, Samaei A, Chen W, Hu A, Choo H, Liaw PK. Lattice distortion in a strong and ductile refractory high-entropy alloy. *Acta Mater*. 2018;160:158.
26. Tsai KY, Tsai MH, Yeh JW. Sluggish diffusion in Co-Cr-Fe-Mn-Ni high-entropy alloys. *Acta Mater*. 2013;61(13):4887.
27. Tsai MH, Yeh JW. High-entropy alloys: a critical review. *Mater Res Lett*. 2014;2(3):107.
28. Zhao S, Stocks G.M, Zhang Y. Defect energetics of concentrated solid-solution alloys from ab initio calculations: Ni<sub>0.5</sub>Co<sub>0.5</sub>Ni<sub>0.5</sub>Fe<sub>0.5</sub>, Ni<sub>0.8</sub>Fe<sub>0.2</sub> and Ni<sub>0.8</sub>Cr<sub>0.2</sub>. *Phys Chem Chem Phys*. 2016;18(34):24043.
29. Lu C, Yang T, Jin K, Gao N, Xiu P, Zhang Y, Gao F, Bei H, Weber WJ, Sun K, Dong Y, Wang L. Radiation-induced segregation on defect clusters in single-phase concentrated solid-solution alloys. *Acta Mater*. 2017;127:98.
30. Sheikh S, Shafeie S, Hu Q, Ahlström J, Persson C, Veselý J, Zýka J, Klement U, Guo S. Alloy design for intrinsically ductile refractory high-entropy alloys. *J Appl Phys*. 2016;120(16):164902.
31. Senkov O, Wilks G, Miracle D, Chuang C, Liaw P. Refractory high-entropy alloys. *Intermetallics*. 2010;18(9):1758.
32. Senkov O, Scott J, Senkova S, Miracle D, Woodward C. Microstructure and room temperature properties of a high-entropy TaNbHfZrTi alloy. *J Alloy Compd*. 2011;509(20):6043.
33. Juan CC, Tsai MH, Tsai CW, Lin CM, Wang WR, Yang CC, Chen SK, Lin SJ, Yeh JW. Enhanced mechanical properties of HfMoTaTiZr and HfMoNbTaTiZr refractory high-entropy alloys. *Intermetallics*. 2015;62:76.
34. Kang B, Lee J, Ryu HJ, Hong SH. Ultra-high strength WNbMo-TaV high-entropy alloys with fine grain structure fabricated by powder metallurgical process. *Mater Sci Eng A*. 2018;712:616.
35. Senkov ON, Miracle DB, Chaput KJ, Couzinie JP. Development and exploration of refractory high entropy alloys—a review. *J Mater Res*. 2018;33(19):3092.
36. Azevedo C. Selection of fuel cladding material for nuclear fission reactors. *Eng Fail Anal*. 2011;18(8):1943.
37. Backman L, Gild J, Luo J, Opila EJ. Part I: theoretical predictions of preferential oxidation in refractory high entropy materials. *Acta Mater*. 2020;197:20.
38. Han Z, Luan H, Liu X, Chen N, Li X, Shao Y, Yao K. Microstructures and mechanical properties of Ti<sub>10</sub>NbMoTaW refractory high-entropy alloys. *Mater Sci Eng A*. 2018;712:380.
39. Zou Y, Maiti S, Steurer W, Spolenak R. Size-dependent plasticity in an Nb<sub>25</sub>Mo<sub>25</sub>Ta<sub>25</sub>W refractory high-entropy alloy. *Acta Mater*. 2014;65:85.
40. Wei S, Kim SJ, Kang J, Zhang Y, Zhang Y, Furuhashi T, Park ES, Tazan CC. Natural-mixing guided design of refractory high-entropy alloys with as-cast tensile ductility. *Nat Mater*. 2020;19(11):1175.
41. Miracle D, Majumdar B, Wertz K, Gorsse S. New strategies and tests to accelerate discovery and development of multi-principal element structural alloys. *Scripta Mater*. 2017;127:195.
42. Senkov O, Miller J, Miracle D, Woodward C. Accelerated exploration of multi-principal element alloys with solid solution phases. *Nat Commun*. 2015;6(1):1.
43. Song H, Tian F, Hu QM, Vitos L, Wang Y, Shen J, Chen N. Local lattice distortion in high-entropy alloys. *Phys Rev Mater*. 2017;1(2):023404.
44. Barrett K, Bragg-Sitton S. Advanced LWR nuclear fuel cladding system development trade-off study. Idaho National Laboratory (INL). Tech. rep. 2012.
45. Brown DA, Chadwick MB, R Capote, Kahler AC, A Trkov, Herman MW, Sonzogni AA, Danon Y, Carlson AD, Dunn M, Smith DL, Hale GM, Arbanas G, Arcilla R, Bates CR, Beck B, Becker B, Brown F, Casperson RJ, Conlin J, Cullen DE, Descalle MA, Firestone R, Gaines T, Guber KH, Hawari AI, Holmes J, Johnson TD, Kawano T, Kiedrowski BC, Koning AJ, Kopecky S, Leal L, Lestone JP, Lubitz C, M´arquez Dami´an JI, Mattoon CM, McCutchan EA, Mughabghab S, Navratil P, Neudecker D, Nobre GBA, Noguere G, M Paris, Pigni MT, Plompen AJ, Pritychenko B, Pronyaev VG, Roubtsov D, Rochman D, Romano P, Schillebeeckx P, Simakov S, Sin M, Sirakov I, Sleaford B, Sobes V, Soukhovitskii ES, Stetcu I, Talou P, Thompson I, van der Marck S, Welser-Sherrill L, Wiarda D, White M, Wormald JL, Wright RQ, Zerkle M, Zerovnik G, Zhu Y. ENDF/B-VIII. 0: the 8th major release of the nuclear reaction data library with CIELO-project cross sections, new standards and thermal scattering data. *Nucl Data Sheets*. 2018;148:1.
46. Chadwick MB, Obložinský P, Herman M, Greene NM, McKnight RD, Smith DL, Young PG, MacFarlane RE, Hale GM,

- Frankle SC, Kahler AC, Kawano T, Little RC, Madland DG, Moller P, Mosteller RD, Page PR, Talou P, Trellue H, White MC, Wilson WB, Arcilla R, Dunford CL, Mughabghab SF, Prytychenko B, Rochman D, Sonzogni AA, Lubitz CR, Trumbull TH, Weinman JP, Brown DA, Cullen DE, Heinrichs DP, McNabb DP, Derrien H, Dunn ME, Larson NM, Leal LC, Carlson AD, Block RC, Briggs JB, Cheng ET, Huria HC, Zerkle ML, Kozier KS, Courcelle A, Pronyaev V, van der Marck SC. ENDF/B-VII. 0: next generation evaluated nuclear data library for nuclear science and technology. Nucl Data Sheets. 2006;107(12):2931.
47. Prince A, Burrows T. Evaluation of natural chromium neutron cross sections for ENDF/BV. Brookhaven National Lab., Upton, NY (USA). Tech. rep. 1979.
  48. Ge Z, Xu R, Wu H, Zhang Y, Chen G, Jin Y, Shu N, Chen Y, Tao X, Tian Y, Liu P, Qian J, Wang JM, Zhang HY, Liu LL, Huang XL. CENDL-3.2: the new version of Chinese general purpose evaluated nuclear data library. In: EPJ Web of Conferences, Vol. 239, EDP Sciences, 2020; p. 09001.
  49. Ge Z, Zhao Z, Xia H, Zhuang Y, Liu T, Zhang J, Wu H. The updated version of Chinese evaluated nuclear data library (CENDL-3.1). J Korean Phys Soc. 2011;59(2):1052.
  50. Cai D, Liang Q, Liu. Chinese evaluated nuclear data library, version 2 (CENDL-2), HeKexue Yu Gongcheng (Chin J Nucl Sci Eng) 1997;17.
  51. Koning AJ, Bauge E, Dean CJ, Dupont E, Fischer U, Forrest RA, Jacqmin R, Leeb H, Kellett MA, Mills RW, Nordborg C, Pescarini M, Rugama Y, Rullhusen P. Status of the JEFF nuclear data library. J Korean Phys Soc. 2011;59(2):1057.
  52. Nakagawa T, Shibata K, Chiba S, Fukahori T, Nakajima Y, Kikuchi Y, Kawano T, Kanda Y, Ohsawa T, Matsunobu H, Kawai M, Zukeran A, Watanabe T, Igarasi S, Kosako K, Asami T. Japanese evaluated nuclear data library version 3 revision-2: JENDL-3.2. J Nucl Sci Technol. 1995;32(12):1259.
  53. Blokhin A, Ignatyuk A, Manokhin V, Nikolaev M. Current status of Russian evaluated neutron data libraries. Institute of Physics and Power Engineering: Tech. rep; 1996.
  54. Koning AJ, Rochman D, Sublet JC, Dzysiuk N, Fleming M, Van Der Marck S. TENDL: complete nuclear data library for innovative nuclear science and technology. Nucl Data Sheets. 2019;155:1.
  55. Forrest R, Tabasso A, Danani C, Jakhar S, Shaw A. Handbook of activation data calculated using EASY-2007. UKAEA FUS. 2009;552:399.
  56. El-Atwani O, Li N, Li M, Devaraj A, Baldwin J, Schneider MM, Sobieraj D, Wróbel JS, Nguyen-Manh D, Maloy SA, Martinez E. Outstanding radiation resistance of tungsten-based high-entropy alloys. Sci Adv. 2019;5(3):eaav2002.
  57. Kareer A, Waite J, Li B, Couet A, Armstrong D, Wilkinson A. low activation, refractory, high entropy alloys for nuclear applications. J Nucl Mater. 2019;526:151744.
  58. Zhang W, Liaw PK, Zhang Y. A novel low-activation VCr-FeTa<sub>x</sub>W<sub>x</sub> (x= 0.1, 0.2, 0.3, 0.4, and 1) high-entropy alloys with excellent heat-softening resistance. Entropy. 2018;20(12):951.
  59. Sun Z, Li X, Wang Z. Microstructure and mechanical properties of low activation Fe-Ti-Cr-V-W multi-principal element alloys. J Nucl Mater. 2020;533:152078.
  60. Waseem OA, Ryu HJ. Toughening of a low-activation tungsten alloy using tungsten short fibers and particles reinforcement for fusion plasma-facing applications. Nucl Fusion. 2018;59(2):026007.
  61. Jia N, Li Y, Liu X, Zheng Y, Wang B, Wang J, Xue Y, Jin K. Thermal stability and mechanical properties of low-activation single-phase Ti-V-Ta medium entropy alloys. JOM. 2019;71(10):3490.
  62. Fazakas E, Zadorozhnyy V, Varga L, Inoue A, Louzguine-Luzgin D, Tian F, Vitos L. Experimental and theoretical study of Ti<sub>20</sub>Zr<sub>20</sub>Hf<sub>20</sub>Nb<sub>20</sub>X<sub>20</sub> (X= V or Cr) refractory high-entropy alloys. Int J Refract Metal Hard Mater. 2014;47:131.
  63. Liliensten L, Couzinié J, Perrière L, Bourgon J, Emery N, Guillot I. New structure in refractory high-entropy alloys. Mater Lett. 2014;132:123.
  64. Fu Z, Chen W, Wen H, Morgan S, Chen F, Zheng B, Zhou Y, Zhang L, Lavernia EJ. Microstructure and mechanical behavior of a novel Co<sub>20</sub>Ni<sub>20</sub>Fe<sub>20</sub>Al<sub>20</sub>Ti<sub>20</sub> alloy fabricated by mechanical alloying and spark plasma sintering. Mater Sci Eng A. 2015;644:10.
  65. Döbelstein H, Thiele M, Gurevich EL, George EP, Ostendorf A. Direct metal deposition of refractory high entropy alloy MoNbTaW. Phys Proc. 2016;83:624.
  66. Feuerbacher M, Lienig T, Thomas C. A single-phase bcc high-entropy alloy in the refractory Zr-Nb-Ti-V-Hf system. Scripta Mater. 2018;152:40.
  67. Han Z, Chen N, Zhao S, Fan L, Yang G, Shao Y, Yao K. Effect of Ti additions on mechanical properties of NbMoTaW and VNbMoTaW refractory high entropy alloys. Intermetallics. 2017;84:153.
  68. Gorr B, Azim M, Christ HJ, Mueller T, Schliephake D, Heilmaier M. Phase equilibria, microstructure, and high temperature oxidation resistance of novel refractory high-entropy alloys. J Alloy Compd. 2015;624:270.
  69. Zhang M, Zhou X, Yu X, Li J. Synthesis and characterization of refractory TiZrNbWMo high-entropy alloy coating by laser cladding. Surf Coat Technol. 2017;311:321.
  70. Stepanov N, Yurchenko NY, Panina E, Tikhonovsky M, Zherbtsov S. Precipitation-strengthened refractory Al<sub>0.5</sub>CrNbTi<sub>2</sub>V<sub>0.5</sub> high entropy alloy. Mater Lett. 2017;188:162.
  71. Wu Y, Cai Y, Wang T, Si J, Zhu J, Wang Y, Hui X. A refractory Hf<sub>25</sub>Nb<sub>25</sub>Ti<sub>25</sub>Zr<sub>25</sub> high-entropy alloy with excellent structural stability and tensile properties. Mater Lett. 2014;130:277.
  72. Maiti S, Steurer W. Structural-disorder and its effect on mechanical properties in single-phase TaNbHfZr high-entropy alloy. Acta Mater. 2016;106:87.
  73. Senkov O, Scott J, Senkova S, Meisenkothen F, Miracle D, Woodward C. Microstructure and elevated temperature properties of a refractory TaNbHfZrTi alloy. J Mater Sci. 2012;47(9):4062.
  74. Guo N, Wang L, Luo L, Li X, Su Y, Guo J, Fu H. Microstructure and mechanical properties of refractory MoNbHfZrTi high-entropy alloy. Mater Des. 2015;81:87.
  75. Guo N, Wang L, Luo L, Li X, Chen R, Su Y, Guo J, Fu H. Microstructure and mechanical properties of *in-situ* MC-carbide particulates-reinforced refractory high-entropy Mo<sub>0.5</sub>NbHf<sub>0.5</sub>ZrTi matrix alloy composite. Intermetallics. 2016;69:74.
  76. Podolskiy A, Tabachnikova E, Voloschuk V, Gorban V, Krapivka N, Firstov S. Mechanical properties and thermally activated plasticity of the Ti<sub>30</sub>Zr<sub>25</sub>Hf<sub>15</sub>Nb<sub>20</sub>Ta<sub>10</sub> high entropy alloy at temperatures 4.2-350 K. Mater Sci Eng A. 2018;710:136.
  77. Liu Y, Zhang Y, Zhang H, Wang N, Chen X, Zhang H, Li Y. Microstructure and mechanical properties of refractory HfMo<sub>0.5</sub>NbTiV<sub>0.5</sub>Si<sub>x</sub> high-entropy composites. J Alloy Compd. 2017;694:869.
  78. Zhang S, Wang Z, Yang H, Qiao J, Wang Z, Wu Y. Ultra-high strain-rate strengthening in ductile refractory high entropy alloys upon dynamic loading. Intermetallics. 2020;121:106699.
  79. Yao H, Qiao JW, Gao MC, Hawk JA, Ma SG, Zhou H. MoNbTaV medium-entropy alloy. Entropy. 2016;18(5):189.
  80. Yao H, Qiao J, Hawk J, Zhou H, Chen M, Gao M. Mechanical properties of refractory high-entropy alloys: experiments and modeling. J Alloy Compd. 2017;696:1139.
  81. Chen SY, Yang X, Dahmen KA, Liaw PK, Zhang Y. Microstructures and crackling noise of Al<sub>x</sub>NbTiMoV high entropy alloys. Entropy. 2014;16(2):870.

82. Zhang Y, Yang X, Liaw P. Alloy design and properties optimization of high-entropy alloys. *JOM*. 2012;64(7):830.
83. Wu Y, Cai Y, Chen X, Wang T, Si J, Wang L, Wang Y, Hui X. Phase composition and solid solution strengthening effect in TiZrNbMoV high-entropy alloys. *Mater Des*. 2015;83:651.
84. Yang X, Zhang Y, Liaw P. Microstructure and compressive properties of NbTiVTaAl<sub>x</sub> high entropy alloys. *Proc Eng*. 2012;36:292.
85. Yao H, Qiao J, Gao M, Hawk J, Ma S, Zhou H, Zhang Y. NbTaV-(Ti, W) refractory high-entropy alloys: experiments and modeling. *Mater Sci Eng A*. 2016;674:203.
86. Chen H, Kauffmann A, Laube S, Choi IC, Schwaiger R, Huang Y, Lichtenberg K, Müller F, Gorr B, Christ HJ, Heilmaier M. Contribution of lattice distortion to solid solution strengthening in a series of refractory high entropy alloys. *Metall Mater Trans A*. 2018;49(3):772.
87. Stepanov N, Shaysultanov D, Salishchev G, Tikhonovsky M. Structure and mechanical properties of a light-weight AlNbTiV high entropy alloy. *Mater Lett*. 2015;142:153.
88. Wang Y, Li B, Ren M, Yang C, Fu H. Microstructure and compressive properties of AlCrFeCoNi high entropy alloy. *Mater Sci Eng A*. 2008;491(1–2):154.
89. Kang B, Kong T, Ryu HJ, Hong S. Superior mechanical properties and strengthening mechanisms of lightweight Al<sub>x</sub>CrNbVMo refractory high-entropy alloys (x = 0, 0.5, 1.0) fabricated by the powder metallurgy process. *J Mater Sci Technol*. 2020;31:2363.
90. Senkov O, Senkova S, Woodward C. Effect of aluminum on the microstructure and properties of two refractory high-entropy alloys. *Acta Mater*. 2014;68:214.
91. Wu Y, Si J, Lin D, Wang T, Wang WY, Wang Y, Liu Z, Hui X. Phase stability and mechanical properties of AlHfNbTiZr high-entropy alloys. *Mater Sci Eng A*. 2018;724:249.
92. Raza A, Kang B, Lee J, Ryu HJ, Hong SH. Transition in microstructural and mechanical behavior by reduction of sigma-forming element content in a novel high entropy alloy. *Mater Des*. 2018;145:11.
93. Chen Y, Xu Z, Wang M, Li Y, Wu C, Yang Y. A single-phase V<sub>0.5</sub>Nb<sub>0.5</sub>ZrTi refractory high-entropy alloy with outstanding tensile properties. *Mater Sci Eng A*. 2020;792:139774.
94. Huang TD, Wu SY, Jiang H, Lu YP, Wang TM, Li TJ. Effect of Ti content on microstructure and properties of Ti<sub>x</sub>ZrVNb refractory high-entropy alloys. *Int J Miner Metall Mater*. 2020;27(10):1318.
95. Qiao DX, Jiang H, Jiao WN, Lu YP, Cao ZQ, Li TJ. A novel series of refractory high-entropy alloys Ti<sub>2</sub>ZrHf<sub>0.5</sub>VNb<sub>x</sub> with high specific yield strength and good ductility. *Acta Metall Sin(English Letters)*. 2019;32(8):925.
96. Pan J, Dai T, Lu T, Ni X, Dai J, Li M. Microstructure and mechanical properties of Nb<sub>25</sub>Mo<sub>25</sub>Ta<sub>25</sub>W<sub>25</sub> and Ti<sub>8</sub>Nb<sub>23</sub>Mo<sub>23</sub>Ta<sub>23</sub>W<sub>23</sub> high entropy alloys prepared by mechanical alloying and spark plasma sintering. *Mater Sci Eng A*. 2018;738:362.
97. Xu Z, Ma Z, Wang M, Chen Y, Tan Y, Cheng X. Design of novel low-density refractory high entropy alloys for high-temperature applications. *Mater Sci Eng A*. 2019;755:318.
98. Wang L, Fu C, Wu Y, Li R, Wang Y, Hui X. Ductile Ti-rich high-entropy alloy controlled by stress induced martensitic transformation and mechanical twinning. *Mater Sci Eng A*. 2019;763:138147.
99. Chen Y, Li Y, Cheng X, Wu C, Cheng B, Xu Z. The microstructure and mechanical properties of refractory high-entropy alloys with high plasticity. *Materials*. 2018;11(2):208.
100. Senkov O, Senkova S, Miracle D, Woodward C. Mechanical properties of low-density, refractory multi-principal element alloys of the Cr-Nb-Ti-V-Zr system. *Mater Sci Eng A*. 2013;565:51.
101. Wang SP, Xu J. (TiZrNbTa)-Mo high-entropy alloys: dependence of microstructure and mechanical properties on Mo concentration and modeling of solid solution strengthening. *Intermetallics*. 2018;95:59.
102. Ge S, Fu H, Zhang L, Mao H, Li H, Wang A, Li W, Zhang H. Effects of Al addition on the microstructures and properties of MoNbTaTiV refractory high entropy alloy. *Mater Sci Eng A*. 2020;784:139275.
103. Waseem OA, Lee J, Lee HM, Ryu HJ. The effect of Ti on the sintering and mechanical properties of refractory high-entropy alloy Ti<sub>x</sub>W<sub>1-x</sub>TaVCr fabricated via spark plasma sintering for fusion plasma-facing materials. *Mater Chem Phys*. 2018;210:87.
104. Gao X, Wang L, Guo N, Luo L, Zhu G, Shi C, Su Y, Guo J. Microstructure characteristics and mechanical properties of Hf<sub>0.5</sub>Mo<sub>0.5</sub>NbTiZr refractory high entropy alloy with Cr addition. *Int J Refract Metals Hard Mater*. 2020;95:105405.
105. Zhou Y, Zhang Y, Wang Y, Chen G. Solid solution alloys of AlCoCrFeNiTi<sub>x</sub> with excellent room-temperature mechanical properties. *Appl Phys Lett*. 2007;90(18):181904.
106. Yurchenko NY, Stepanov N, Zherebtsov S, Tikhonovsky M, Salishchev G. Structure and mechanical properties of B2 ordered refractory AlNbTiVZr<sub>x</sub> (x = 0–1.5) high-entropy alloys. *Mater Sci Eng A*. 2017;704:82.
107. Huang H, Wu Y, He J, Wang H, Liu X, An K, Wu W, Lu Z. Phase-transformation ductilization of brittle high-entropy alloys via metastability engineering. *Adv Mater*. 2017;29(30):1701678.
108. Guo N, Wang L, Luo L, Li X, Chen R, Su Y, Guo J, Fu H. Microstructure and mechanical properties of refractory high entropy (Mo<sub>0.5</sub>NbHf<sub>0.5</sub>ZrTi) BCC/M<sub>5</sub>Si<sub>3</sub> *in-situ* compound. *J Alloy Compd*. 2016;660:197.
109. Zhang Y, Liu Y, Li Y, Chen X, Zhang H. Microstructure and mechanical properties of a refractory HfNbTiVSi<sub>0.5</sub> high-entropy alloy composite. *Mater Lett*. 2016;174:82.
110. Ma Y, Jiang B, Li C, Wang Q, Dong C, Liaw PK, Xu F, Sun L. The BCC/B2 morphologies in Al<sub>x</sub>NiCoFeCr high-entropy alloys. *Metals*. 2017;7(2):57.
111. Senkov O, Woodward C, Miracle D. Microstructure and properties of aluminum-containing refractory high-entropy alloys. *JOM*. 2014;66(10):2030.
112. Zhou Y, Jin X, Zhang L, Du X, Li B. A hierarchical nanostructured Fe<sub>34</sub>Cr<sub>34</sub>Ni<sub>14</sub>Al<sub>14</sub>Co<sub>4</sub> high-entropy alloy with good compressive mechanical properties. *Mater Sci Eng A*. 2018;716:235.
113. Soni V, Senkov O, Couzinie JP, Zheng Y, Gwalani B, Banerjee R. Phase stability and microstructure evolution in a ductile refractory high entropy alloy Al<sub>10</sub>Nb<sub>15</sub>Ta<sub>5</sub>Ti<sub>30</sub>Zr<sub>40</sub>. *Materialia*. 2020;9:100569.
114. Wang Q, Ma Y, Jiang B, Li X, Shi Y, Dong C, Liaw PK. A cuboidal B2 nanoprecipitation-enhanced body-centered-cubic alloy Al<sub>0.7</sub>CoCrFe<sub>2</sub>Ni with prominent tensile properties. *Scripta Mater*. 2016;120:85.
115. Gong X, Xiang C, Auger T, Chen J, Liang X, Yu Z, Short MP, Song M, Yin Y. Liquid metal embrittlement of a dual-phase Al<sub>0.7</sub>CoCrFeNi high-entropy alloy exposed to oxygen-saturated lead-bismuth eutectic. *Scripta Mater*. 2021;194:113652.
116. Ng C, Guo S, Luan J, Wang Q, Lu J, Shi S, Liu C. Phase stability and tensile properties of Co-free Al<sub>0.5</sub>CrCuFeNi<sub>2</sub> high-entropy alloys. *J Alloy Compd*. 2014;584:530.
117. Kuznetsov AV, Shaysultanov DG, Stepanov ND, Salishchev GA, Senkov ON. Tensile properties of an AlCrCuNiFeCo high-entropy alloy in as-cast and wrought conditions. *Mater Sci Eng A*. 2012;533:107.
118. Senkov O, Jensen J, Pilchak A, Miracle D, Fraser H. Compositional variation effects on the microstructure and properties of a refractory high-entropy superalloy AlMo<sub>0.5</sub>NbTa<sub>0.5</sub>TiZr. *Mater Des*. 2018;139:498.

119. Lin CM, Juan CC, Chang CH, Tsai CW, Yeh JW. Effect of Al addition on mechanical properties and microstructure of refractory  $\text{Al}_x\text{HfNbTaTiZr}$  alloys. *J Alloy Compd.* 2015;624:100.
120. Senkov ON, Senkova SV, Woodward C, Miracle DB. Low-density, refractory multi-principal element alloys of the Cr-Nb-Ti-V-Zr system: Microstructure and phase analysis. *Acta Mater.* 2013;61(5):1545.
121. Jiang H, Jiang L, Lu YP, Wang TM, Cao ZQ, Li TJ. Microstructure and mechanical properties of the W-Ni-Co system refractory high-entropy alloys. In: *Materials Science Forum*, Vol. 816, Trans Tech Publ; 2015; p. 324.
122. Wen L, Kou H, Li J, Chang H, Xue X, Zhou L. Effect of aging temperature on microstructure and properties of  $\text{AlCoCrCuFeNi}$  high-entropy alloy. *Intermetallics.* 2009;17(4):266.
123. Xiang C, Zhang Z, Fu H, Han EH, Zhang H, Wang J. Microstructure and corrosion behavior of  $\text{AlCoCrFeNiSi}_{0.1}$  high-entropy alloy. *Intermetallics.* 2019;114:106599.
124. Yang CC, Chau JH, Weng CJ, Chen CS, Chou YH. Preparation of high-entropy  $\text{AlCoCrCuFeNiSi}$  alloy powders by gas atomization process. *Mater Chem Phys.* 2017;202:151.
125. Munitz A, Meshi L, Kaufman M. Heat treatments' effects on the microstructure and mechanical properties of an equiatomic Al-Cr-Fe-Mn-Ni high entropy alloy. *Mater Sci Eng A.* 2017;689:384.
126. Alshataif YA, Sivasankaran S, Al-Mufadi FA, Alaboodi AS, Ammar HR. Manufacturing methods, microstructural and mechanical properties evolutions of high-entropy alloys: a review. *Metals Mater Int.* 2019;26:1.
127. Vaidya M, Muralikrishna GM, Murty BS. High-entropy alloys by mechanical alloying: a review. *J Mater Res.* 2019;34(5):664.
128. Joseph J, Imran M, Hodgson P, Barnett M, Fabijanic D. Towards the large-scale production and strength prediction of near-eutectic  $\text{Al}_x\text{CoCrFeNi}_{2.1}$  alloys by additive manufacturing. *Manuf Lett.* 2020;25:16.
129. Lu Y, Dong Y, Guo S, Jiang L, Kang H, Wang T, Wen B, Wang Z, Jie J, Cao Z, Ruan H, Li T. A promising new class of high-temperature alloys: eutectic high-entropy alloys. *Sci Rep.* 2014;4(1):1.
130. Lu Y, Gao X, Jiang L, Chen Z, Wang T, Jie J, Kang H, Zhang Y, Guo S, Ruan H, Zhao Y, Cao Z, Li T. Directly cast bulk eutectic and near-eutectic high entropy alloys with balanced strength and ductility in a wide temperature range. *Acta Mater.* 2017;124:143.
131. Xu S, Amirkhiz BS. Mechanical properties of fuel cladding candidate alloys for Canadian SCWR concept. *JOM.* 2016;68(2):469.
132. Zheng W, Guzonas D, Boyle KP, Li J, Xu S. Materials assessment for the Canadian SCWR core concept. *JOM.* 2016;68(2):456.
133. Zinkle SJ. Opportunities and challenges for materials innovation in nuclear energy. In: *EPJ Web of Conferences*, Vol. 51, EDP Sciences; 2013; p. 01001.
134. Zinkle SJ, Ghoniem NM. Prospects for accelerated development of high performance structural materials. *J Nucl Mater.* 2011;417(1–3):2.
135. Song M, Sun C, Fan Z, Chen Y, Zhu R, Yu K, Hartwig K, Wang H, Zhang X. A roadmap for tailoring the strength and ductility of ferritic/martensitic T91 steel via thermo-mechanical treatment. *Acta Mater.* 2016;112:361.
136. Kim SH, Ryu WS, Kuk IH. Microstructure and mechanical properties of Cr-Mo steels for nuclear industry applications. *Nucl Eng Technol.* 1999;31(6):561.
137. Gupta G, Jiao Z, Ham A, Busby J, Was G. Microstructural evolution of proton irradiated T91. *J Nucl Mater.* 2006;351(1–3):162.
138. Pugh S. XCII. Relations between the elastic moduli and the plastic properties of polycrystalline pure metals. *Lond Edinb Philos Mag J Sci.* 1954;45(367):823.
139. Pettifor D. Theoretical predictions of structure and related properties of intermetallics. *Mater Sci Technol.* 1992;8(4):345.
140. Senkov ON, Isheim D, Seidman DN, Pilchak AL. Development of a refractory high entropy superalloy. *Entropy.* 2016;18(3):102.
141. Chen H, Kauffmann A, Gorr B, Schliephake D, Seemüller C, Wagner J, Christ HJ, Heilmaier M. Microstructure and mechanical properties at elevated temperatures of a new Al-containing refractory high-entropy alloy Nb-Mo-Cr-Ti-Al. *J Alloy Compd.* 2016;661:206.
142. Labusch R. Statistical theories of solid solution hardening (concentration of solute atoms, interaction range between solute atoms and distortion, and interaction strength of solid solution hardening). *Acta Met (London).* 1972;20:917.
143. Toda-Caraballo I, Rivera-Díaz-del Castillo PE. Modelling solid solution hardening in high entropy alloys. *Acta Mater.* 2015;85:14.
144. Juan CC, Tseng KK, Hsu WL, Tsai MH, Tsai CW, Lin CM, Chen SK, Lin SJ, Yeh JW. Solution strengthening of ductile refractory  $\text{HfMo}_x\text{NbTaTiZr}$  high-entropy alloys. *Mater Lett.* 2016;175:284.
145. George EP, Curtin W, Tazan CC. High entropy alloys: a focused review of mechanical properties and deformation mechanisms. *Acta Mater.* 2020;188:435.
146. Rao S, Varvenne C, Woodward C, Parthasarathy T, Miracle D, Senkov O, Curtin W. Atomistic simulations of dislocations in a model BCC multicomponent concentrated solid solution alloy. *Acta Mater.* 2017;125:311.
147. Rao S, Akdim B, Antillon E, Woodward C, Parthasarathy T, Senkov O. Modeling solution hardening in BCC refractory complex concentrated alloys:  $\text{NbTiZr}$ ,  $\text{Nb}_{1.5}\text{TiZr}_{0.5}$  and  $\text{Nb}_{0.5}\text{TiZr}_{1.5}$ . *Acta Mater.* 2019;168:222.
148. Rao S, Antillon E, Woodward C, Akdim B, Parthasarathy T, Senkov O. Solution hardening in body-centered cubic quaternary alloys interpreted using Suzuki's kink-solute interaction model. *Scripta Mater.* 2019;165:103.
149. Chen Y, Li Y, Cheng X, Xu Z, Wu C, Cheng B, Wang M. Interstitial strengthening of refractory  $\text{ZrTiHfNb}_{0.5}\text{Ta}_{0.5}\text{O}_x$  ( $x = 0.05, 0.1, 0.2$ ) high-entropy alloys. *Mater Lett.* 2018;228:145.
150. Juan CC, Tsai MH, Tsai CW, Hsu WL, Lin CM, Chen SK, Lin SJ, Yeh JW. Simultaneously increasing the strength and ductility of a refractory high-entropy alloy via grain refining. *Mater Lett.* 2016;184:200.
151. Yang D, Liu Y, Jiang H, Liao M, Qu N, Han T, Lai Z, Zhu J. A novel  $\text{FeCrNiAlTi}$ -based high entropy alloy strengthened by refined grains. *J Alloy Compd.* 2020;823:153729.
152. Baldan A. Review progress in Ostwald ripening theories and their applications to the  $\gamma'$ -precipitates in nickel-base superalloys part II nickel-base superalloys. *J Mater Sci.* 2002;37(12):2379.
153. Stepanov N, Yurchenko NY, Zharebtsov S, Tikhonovsky M, Salishchev G. Aging behavior of the  $\text{HfNbTaTiZr}$  high entropy alloy. *Mater Lett.* 2018;211:87.
154. Wang Q, Han J, Liu Y, Zhang Z, Dong C, Liaw PK. Coherent precipitation and stability of cuboidal nanoparticles in body-centered-cubic  $\text{Al}_{0.4}\text{Nb}_{0.5}\text{Ta}_{0.5}\text{TiZr}_{0.8}$  refractory high entropy alloy. *Scripta Mater.* 2020;190:40.
155. Soni V, Gwalani B, Senkov ON, Viswanathan B, Alam T, Miracle DB, Banerjee R. Phase stability as a function of temperature in a refractory high-entropy alloy. *J Mater Res.* 2018;33(19):3235.
156. Chen ST, Tang WY, Kuo YF, Chen SY, Tsau CH, Shun TT, Yeh JW. Microstructure and properties of age-hardenable  $\text{Al}_x\text{CrFe}_{1.5}\text{MnNi}_{0.5}$  alloys. *Mater Sci Eng A.* 2010;527(21–22):5818.
157. Ren B, Liu Z, Cai B, Wang M, Shi L. Aging behavior of a  $\text{CuCr}_2\text{Fe}_2\text{NiMn}$  high-entropy alloy. *Mater Des.* 2012;33:121.
158. Zhang Y, Jin K, Xue H, Lu C, Olsen RJ, Beland LK, Ullah MW, Zhao S, Bei H, Aidhy DS, Samolyuk GD, Wang L, Caro M, Caro A, Stocks GM, Larson BC, Robertson IM, Correa AA, Weber



- WJ. Influence of chemical disorder on energy dissipation and defect evolution in advanced alloys, *J Mater Res.* 31(16):2363.
159. Jin K, Bei H, Zhang Y. Ion irradiation induced defect evolution in Ni and Ni-based FCC equiatomic binary alloys. *J Nucl Mater.* 2016;471:193.
  160. Granberg F, Nordlund K, Ullah MW, Jin K, Lu C, Bei H, Wang L, Djurabekova F, Weber W, Zhang Y. Mechanism of radiation damage reduction in equiatomic multicomponent single phase alloys. *Phys Rev Lett.* 2016;116(13):135504.
  161. He MR, Wang S, Jin K, Bei H, Yasuda K, Matsumura S, Higashida K, Robertson IM. Enhanced damage resistance and novel defect structure of FeCoNi under in situ electron irradiation. *Scripta Mater.* 2016;125:5.
  162. Chen D, Tong Y, Li H, Wang J, Zhao Y, Hu A, Kai J. Helium accumulation and bubble formation in FeCoNiCr alloy under high fluence He<sup>+</sup> implantation. *J Nucl Mater.* 2018;501:208.
  163. Yan Z, Liu S, Xia S, Zhang Y, Wang Y, Yang T. He behavior in Ni and Ni-based equiatomic solid solution alloy. *J Nucl Mater.* 2018;505:200.
  164. Fukumoto K, Kimura A, Matsui H. Swelling behavior of V-Fe binary and V-Fe-Ti ternary alloys. *J Nucl Mater.* 1998;258:1431.
  165. Yoshiie T, Xu Q, Satoh Y, Ohkubo H, Kiritani M. The effect of alloying elements on the defect structural evolution in neutron irradiated Ni alloys. *J Nucl Mater.* 2000;283:229.
  166. Li QJ, Sheng H, Ma E. Strengthening in multi-principal element alloys with local-chemical-order roughened dislocation pathways. *Nat Commun.* 2019;10(1):1.
  167. Senkov O, Miracle D. Effect of the atomic size distribution on glass forming ability of amorphous metallic alloys. *Mater Res Bull.* 2001;36(12):2183.
  168. Chen B, Li S, Zong H, Ding X, Sun J, Ma E. Unusual activated processes controlling dislocation motion in body-centered-cubic high-entropy alloys. *Proc Nat Acad Sci.* 2020;117(28):16199.
  169. Ma E. Unusual dislocation behavior in high-entropy alloys. *Scripta Mater.* 2020;181:127.
  170. Zhao S. Defect properties in a VTaCrW equiatomic high entropy alloy (HEA) with the body centered cubic (bcc) structure. *J Mater Sci Technol.* 2020;44:133.
  171. Parkin C, Moorehead M, Elbakhshwan M, Hu J, Chen W-Y, Li M, He L, Sridharan K, Couet A. In situ microstructural evolution in face-centered and body-centered cubic complex concentrated solid-solution alloys under heavy ion irradiation. *Acta Mater.* 2020;198:85.
  172. Nagase T, Takeuchi A, Amiya K, Egami T. Solid state amorphization of metastable Al<sub>0.5</sub>TiZrPdCuNi high entropy alloy investigated by high voltage electron microscopy. *Mater Chem Phys.* 2018;210:291.
  173. Sadeghilaridjani M, Ayyagari A, Muskeri S, Hasannaeimi V, Salloom R, Chen WY, Mukherjee S. Ion irradiation response and mechanical behavior of reduced activity high entropy alloy. *J Nucl Mater.* 2020;529:151955.
  174. Lu Y, Huang H, Gao X, Ren C, Gao J, Zhang H, Zheng S, Jin Q, Zhao Y, Lu C, Wang T, Li T. A promising new class of irradiation tolerant materials: high-entropy alloy Ti<sub>2</sub>ZrHfV<sub>0.5</sub>Mo<sub>0.2</sub>. *J Mater Sci Technol.* 2019;35(3):369.
  175. Patel D, Richardson MD, Jim B, Akhmadaliev S, Goodall R, Gandy AS. Radiation damage tolerance of a novel metastable refractory high entropy alloy V<sub>2.5</sub>Cr<sub>1.2</sub>WMoCo<sub>0.04</sub>. *J Nucl Mater.* 2020;531:152005.
  176. Chang S, Tseng KK, Yang TY, Chao DS, Yeh JW, Liang JH. Irradiation-induced swelling and hardening in HfNbTaTiZr refractory high-entropy alloy. *Mater Lett.* 2020;272:127832.
  177. Odbadrakh K, Enkhtor L, Amartaivan T, Nicholson D, Stocks GM, Egami T. Electronic structure and atomic level complexity in Al<sub>0.5</sub>TiZrPdCuNi high-entropy alloy in glass phase. *J Appl Phys.* 2019;126(9):095104.
  178. Nagase T, Anada S, Rack PD, Noh JH, Yasuda H, Mori H, Egami T. Electron-irradiation-induced structural change in Zr-Hf-Nb alloy. *Intermetallics.* 2012;26:122.
  179. Xu C, Chen WY, Chen Y, Yang Y. Microstructural evolution of NF709 austenitic stainless steel under in-situ ion irradiations at room temperature, 300, 400, 500 and 600 °C. *J Nucl Mater.* 2018;509:644.
  180. El-Atwani O, Esquivel E, Aydogan E, Martinez E, Baldwin J, Li M, Uberuaga BP, Maloy SA. Unprecedented irradiation resistance of nanocrystalline tungsten with equiaxed nanocrystalline grains to dislocation loop accumulation. *Acta Mater.* 2019;165:118.
  181. Wang Z, Liu C, Dou P. Thermodynamics of vacancies and clusters in high-entropy alloys. *Phys Rev Mater.* 2017;1(4):043601.
  182. Xia S, Yang X, Yang T, Liu S, Zhang Y. Irradiation resistance in Al<sub>x</sub>CoCrFeNi high entropy alloys. *JOM.* 2015;67(10):2340.
  183. Jiang L, Hu YJ, Sun K, Xiu P, Song M, Zhang Y, Boldman WL, Crespillo ML, Rack PD, Qi L, Weber WJ, Lumin W. Irradiation-induced extremes create hierarchical face-/body-centered-cubic phases in nanostructured high entropy alloys. *Adv Mater.* 2020;32(39):2002652.
  184. Egami T, Guo W, Rack P, Nagase T. Irradiation resistance of multicomponent alloys. *Metall Mater Trans A.* 2014;45(1):180.
  185. Murty K, Charit I. Structural materials for Gen-IV nuclear reactors: challenges and opportunities. *J Nucl Mater.* 2008;383(1–2):189.
  186. Allen T, Crawford D. Lead-cooled fast reactor systems and the fuels and materials challenges. *Sci Technol Nucl Install.* 2007;2007:1.
  187. Kurata Y, Futakawa M. Excellent corrosion resistance of 18Cr-20Ni-5Si steel in liquid Pb-Bi. *J Nucl Mater.* 2004;325(2–3):217.
  188. Short M, Ballinger R, Hänninen H. Corrosion resistance of alloys F91 and Fe-12Cr-2Si in lead-bismuth eutectic up to 715 °C. *J Nucl Mater.* 2013;434(1–3):259.
  189. Zhang W, Tang R, Yang Z, Liu C, Chang H, Yang J, Liao J, Yang Y, Liu N. Preparation, structure, and properties of an AlCrMoNbZr high-entropy alloy coating for accident-tolerant fuel cladding. *Surf Coat Technol.* 2018;347:13.
  190. Tao Z, Wang P, Wang C, Ma Z, Zhang Y, Xue F, Bai G, Yuan Y, Lan R. Design and characterisation of AlCrFeCuNb<sub>x</sub> alloys for accident-tolerant fuel cladding. *J Alloys Compd.* 2020;859:157805.
  191. Taylor C. D, Lu P, Saal J, Frankel G, Scully J. Integrated computational materials engineering of corrosion resistant alloys. *npj Mater Degrad.* 2018;2(2):1.
  192. Zhou Q, Sheikh S, Ou P, Chen D, Hu Q, Guo S. Corrosion behavior of Hf<sub>0.5</sub>Nb<sub>0.5</sub>Ta<sub>0.5</sub>Ti<sub>1.5</sub>Zr refractory high-entropy in aqueous chloride solutions. *Electrochem Commun.* 2019;98:63.
  193. Li M, Chen Q, Cui X, Peng X, Huang G. Evaluation of corrosion resistance of the single-phase light refractory high entropy alloy TiCrVNB<sub>0.5</sub>Al<sub>0.5</sub> in chloride environment. *J Alloys Compd.* 2020;857:158278.
  194. Patel NS, Pavlík V, Boča M. High-temperature corrosion behavior of superalloys in molten salts—a review. *Crit Rev Solid State Mater Sci.* 2017;42(1):83.
  195. Bachani SK, Wang CJ, Lou BS, Chang LC, Lee JW. Microstructural characterization, mechanical property and corrosion behavior of VNbMoTaWAl refractory high entropy alloy coatings: Effect of Al content. *Surf Coat Technol.* 2020;403:126351.
  196. Hung SB, Wang CJ, Chen YY, Lee JW, Li CL. Thermal and corrosion properties of V-Nb-Mo-Ta-W and V-Nb-Mo-Ta-W-Cr-B high entropy alloy coatings. *Surf Coat Technol.* 2019;375:802.

197. Li J, Yang X, Zhu R. Corrosion and sarration behaviors of  $\text{TiZr}_{0.5}\text{NbCr}_{0.5}\text{V}_x\text{Mo}_y$  high entropy alloys in aqueous environments. *Metals*. 2014;4(4):597.
198. Shi Y, Yang B, Xie X, Brecht J, Dahmen KA, Liaw PK. Corrosion of  $\text{Al}_x\text{CoCrFeNi}$  high-entropy alloys: Al-content and potential scan-rate dependent pitting behavior. *Corros Sci*. 2017;119:33.
199. Kao YF, Lee TD, Chen SK, Chang YS. Electrochemical passive properties of  $\text{Al}_x\text{CoCrFeNi}$  ( $x=0, 0.25, 0.50, 1.00$ ) alloys in sulfuric acids. *Corros Sci*. 2010;52(3):1026.
200. Lee C, Chang C, Chen Y, Yeh J, Shih H. Effect of the aluminium content of  $\text{Al}_x\text{CrFe}_{1.5}\text{MnNi}_{0.5}$  high-entropy alloys on the corrosion behaviour in aqueous environments. *Corros Sci*. 2008;50(7):2053.
201. Shih H. C, Lee C. P, Chen Y, Wu C, Hsu C, Yeh J. Effect of boron on the corrosion properties of  $\text{Al}_{0.5}\text{CoCrCuFeNiB}_x$  high entropy alloys in 1N sulfuric acid. *ECS Trans*. 2007;2(26):15.
202. Frankel G. Pitting corrosion of metals: a review of the critical factors. *J Electrochem Soc*. 1998;145(6):2186.
203. Jayaraj J, Thinaharan C, Ningshen S, Mallika C, Mudali UK. Corrosion behavior and surface film characterization of tanbhfzrti high entropy alloy in aggressive nitric acid medium. *Intermetallics*. 2017;89:123.
204. Li Q, Yue T, Guo Z, Lin X. Microstructure and corrosion properties of  $\text{AlCoCrFeNi}$  high entropy alloy coatings deposited on AISI 1045 steel by the electrospray process. *Metall Mater Trans A*. 2013;44(4):1767.
205. Yang Y, Fan X, Wang F, Qi H, Yue Y, Ma M, Zhang X, Li G, Liu R. Effect of Nb content on corrosion behavior of Ti-based bulk metallic glass composites in different solutions. *Appl Surf Sci*. 2019;471:108.
206. Lee C, Chen Y, Hsu C, Yeh J, Shih H. The effect of boron on the corrosion resistance of the high entropy alloys  $\text{Al}_{0.5}\text{CoCrCuFeNiB}_x$ . *J Electrochem Soc*. 2007;154(8):C424.

metals and semiconductors, neutron scintillator characterization, and radiation shielding and protection.



**Dr. Chen-Yang Lu** is now a professor in the Department of Nuclear Science and Technology of Xi'an Jiaotong University. He received his Ph.D. in Materials Science from Northeastern University in 2014. He worked at the University of Michigan as a post-doctoral fellow and research scientist in the Department of Nuclear Engineering & Radiological Sciences from 2014 to 2018. Prof. Lu engaged in the research of nuclear engineering materials. He focused his researches on the preparation of

advanced nuclear structural materials, radiation damages in materials, and advanced microstructural characterizations. He has published more than 40 SCI peer-reviewed papers, including 4 *Nature Communications*, 4 *Acta Materialia*, 10 *Journal of Nuclear Materials* and other related influential papers in this field. The articles have been cited more than 2,100 times with a h-index of 23.

**Publisher's Note** Springer Nature remains neutral with regard to jurisdictional claims in published maps and institutional affiliations.



**Dr. Tan Shi** is now an assistant professor at the Department of Nuclear Science and Technology of Xi'an Jiaotong University, China. He received his M.S. degree in Nuclear Engineering at the Institute for Nuclear Science and Technology, France in 2014 and Ph.D. degree in Nuclear Engineering at the Department of Nuclear Engineering and Radiological Sciences at University of Michigan, United States in 2019. Dr. Shi engaged in the research of radiation effects on